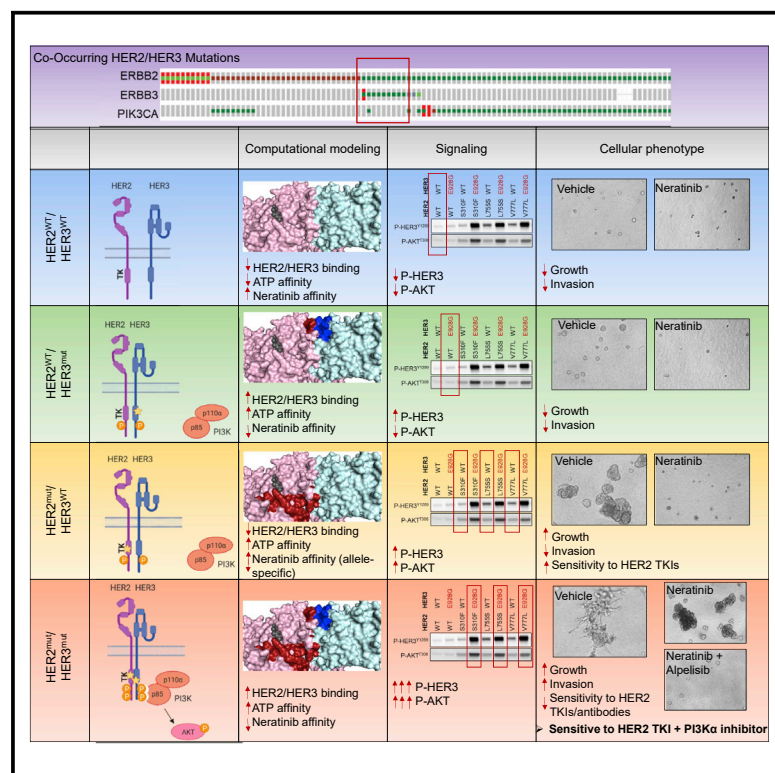


Co-occurring gain-of-function mutations in *HER2* and *HER3* modulate *HER2/HER3* activation, oncogenesis, and *HER2* inhibitor sensitivity

Graphical abstract



Authors

Ariella B. Hanker, Benjamin P. Brown, Jens Meiler, ..., Jie He, Alshad S. Lalani, Carlos L. Arteaga

Correspondence

ariella.hanker@utsouthwestern.edu

In brief

Hanker and Brown et al. demonstrate that co-occurring *HER2* and *HER3* mutations cooperatively activate *HER2/HER3* and *PI3K* signaling in tumor cells, leading to enhanced growth, invasion, and resistance to *HER2* inhibitors. *HER2/HER3* double-mutant tumor models are sensitive to the combination of a *HER2* TKI and a *PI3Kα* inhibitor.

Highlights

- Co-occurring *HER2/HER3* mutations promote oncogenesis and invasion via *PI3K* activation
- *HER3* mutations reduce sensitivity to *HER2* inhibitors in *HER2*-mutant cancer cells
- Tumors with *HER2/HER3* mutations are sensitive to *HER2* TKI + *PI3Kα* inhibitor



Article

Co-occurring gain-of-function mutations in *HER2* and *HER3* modulate *HER2/HER3* activation, oncogenesis, and *HER2* inhibitor sensitivity

Ariella B. Hanker,^{1,2,12,13,*} Benjamin P. Brown,^{3,12} Jens Meiler,^{4,5,12} Arnaldo Marín,^{1,6} Harikrishna S. Jayanthan,⁴ Dan Ye,¹ Chang-Ching Lin,¹ Hiroaki Akamatsu,¹ Kyung-Min Lee,^{1,7} Sumanta Chatterjee,¹ Dhivya R. Sudhan,¹ Alberto Servetto,¹ Monica Red Brewer,⁴ James P. Koch,⁸ Jonathan H. Sheehan,⁹ Jie He,¹⁰ Alshad S. Lalani,¹¹ and Carlos L. Arteaga^{1,2}

¹UTSW Simmons Comprehensive Cancer Center, Dallas, 5323 Harry Hines Boulevard, TX 75390, USA

²Department of Internal Medicine, UT Southwestern Medical Center, Dallas, TX 75390, USA

³Chemical and Physical Biology Program, Center for Structural Biology, and Medical Scientist Training Program, Vanderbilt University, Nashville, TN 37240, USA

⁴Department of Chemistry and Center for Structural Biology, Vanderbilt University, Nashville, TN 37240, USA

⁵Institute for Drug Discovery, Leipzig University Medical School, Leipzig, SAC 04103, Germany

⁶Doctoral Program in Medical Sciences, Faculty of Medicine, University of Chile, Santiago 8380453, Chile

⁷Department of Life Sciences, College of Natural Science, Hanyang University, Seoul 04736, Republic of Korea

⁸Department of Medicine, Vanderbilt University Medical Center, Nashville, TN 37232, USA

⁹Division of Infectious Diseases, Department of Internal Medicine, Washington University School of Medicine, St. Louis, MO 63110, USA

¹⁰Foundation Medicine, Cambridge, MA 02141, USA

¹¹Puma Biotechnology, Inc., Los Angeles, CA 90024, USA

¹²These authors contributed equally

¹³Lead contact

*Correspondence: ariella.hanker@utsouthwestern.edu

<https://doi.org/10.1016/j.ccell.2021.06.001>

SUMMARY

Activating mutations in *HER2* (*ERBB2*) drive the growth of a subset of breast and other cancers and tend to co-occur with *HER3* (*ERBB3*) missense mutations. The *HER2* tyrosine kinase inhibitor neratinib has shown clinical activity against *HER2*-mutant tumors. To characterize the role of *HER3* mutations in *HER2*-mutant tumors, we integrate computational structural modeling with biochemical and cell biological analyses. Computational modeling predicts that the frequent *HER3*^{E928G} kinase domain mutation enhances the affinity of *HER2/HER3* and reduces binding of *HER2* to its inhibitor neratinib. Co-expression of mutant *HER2/HER3* enhances *HER2/HER3* co-immunoprecipitation and ligand-independent activation of *HER2/HER3* and *PI3K/AKT*, resulting in enhanced growth, invasiveness, and resistance to *HER2*-targeted therapies, which can be reversed by combined treatment with *PI3Kα* inhibitors. Our results provide a mechanistic rationale for the evolutionary selection of co-occurring *HER2/HER3* mutations and the recent clinical observations that *HER3* mutations are associated with a poor response to neratinib in *HER2*-mutant cancers.

INTRODUCTION

Activating mutations in *HER2* (also known as *ERBB2*) are oncogenic drivers in a subset of breast and other cancers (Bose et al., 2013; Hanker et al., 2017; Hyman et al., 2018). In breast cancer, *HER2* mutations typically occur in the absence of *HER2* amplification, are more common in invasive lobular breast cancer (Deniziaut et al., 2016; Desmedt et al., 2016; Ping et al., 2016; Ross et al., 2013), and are associated with poor prognosis (Kurozumi et al., 2020; Ping et al., 2016; Wang et al., 2017). Recurrent *HER2* mutations promote resistance to antiestrogen therapy in estrogen receptor-positive (ER+) breast cancers (Croessmann et al., 2019; Nayar et al., 2019) and are found in ~5% of endocrine-resistant metastatic breast cancers (Razavi et al., 2018). They have also been implicated in resistance to *HER2* inhibitors in

HER2-amplified breast cancers (Cocco et al., 2018; Xu et al., 2017) and can be targeted with *HER2* tyrosine kinase inhibitors (TKIs), such as neratinib. Approximately 30% of *HER2*-mutant metastatic breast cancers respond to neratinib (Hyman et al., 2018), suggesting that co-occurring mutations may modulate *HER2* TKI response.

HER2 is a member of the *ERBB* receptor tyrosine kinase family, which includes *EGFR*, *HER3* (*ERBB3*), and *HER4* (*ERBB4*). Upon ligand-induced homo- and heterodimerization of the extracellular domain (ECD), *ERBB* receptors undergo a conformational change that triggers asymmetric dimerization of the kinase domains (KDs), leading to kinase activation and subsequent signal transduction through oncogenic pathways, such as the phosphoinositide-3-kinase (*PI3K*)/*AKT*/mTOR and *RAS*/*RAF*/MEK/*ERK* pathways (Zhang et al., 2006). Although *HER2* lacks



a high-affinity ligand, its natural conformation resembles a ligand-activated state and is the preferred heterodimer of EGFR and HER3 (Arteaga and Engelman, 2014). HER3 is catalytically impaired and its signaling depends on heterodimerization with catalytically active partner, such as EGFR and HER2 (Wallasch et al., 1995).

The most common *HER2* mutations in breast cancer are missense mutations in the KDs, such as *HER2*^{L755S} and *HER2*^{V777L}. While *HER2* missense mutants exhibit gain-of-function activity (Bose et al., 2013), they are not potentially transforming in the absence of amplification and may require cooperation with other oncogenes to confer a fully transformed phenotype. For example, co-occurring *PIK3CA* mutations (encoding PI3K) cooperate with *HER2* mutations to augment pathway activation (Zabransky et al., 2015). However, *PIK3CA* mutations are only found in ~1/3 of *HER2*-mutant breast cancers; other alterations that cooperate with *HER2* mutations are not known.

Gain-of-function mutations in *HER3* are found in ~2% of breast cancers (Cancer Genome Atlas, 2012; Jaiswal et al., 2013). *HER2/HER3* heterodimers exhibit high catalytic activity, strongly activate the PI3K/AKT/mTOR pathway, and induce transformation more potently than any other ERBB dimers (Choi et al., 2020; Holbro et al., 2003; Yarden and Sliwkowski, 2001). In the *HER2/HER3* asymmetric dimer, the *HER3* KD serves as the “activator,” stimulating the kinase activity of the *HER2* “receiver” (Choi et al., 2020). Co-occurring *HER3* mutations have previously been found in *HER2*-mutant tumors (Hanker et al., 2017) and are associated with lower clinical response to neratinib in the clinic (Hyman et al., 2018; Smyth et al., 2020). We hypothesized that the mutant *HER3* receptor cooperates with mutant *HER2* to promote tumor growth via enhanced *HER2* and PI3K activation.

RESULTS

Activating mutations in *HER2* and *HER3* co-occur in breast and other cancers

We interrogated 277 breast cancers (Figures 1A and S1A) and 1,561 pan-cancers harboring somatic *HER2* mutations from the Project GENIE dataset (genie.cBioPortal.org) for co-occurring alterations in *EGFR*, *ERBB3*, *ERBB4*, *PIK3CA*, and *PTEN* (Figures 1B and S1B). Since *HER2* mutations are known to be associated with lobular breast cancer (Desmedt et al., 2016), we also included the *CDH1* gene, which is mutated frequently in lobular breast cancer. Mutations in *HER2* and *HER3* showed a significant tendency to co-occur in breast cancer ($q = 0.006$) and in all cancers ($q = 1.01 \times 10^{-26}$; Figures 1C and S1C). Most co-occurrences were between known activating missense mutations in both genes rather than variants of unknown significance (Figures S1A and S1B). In breast cancer, neither *EGFR* nor *ERBB4* alterations were found to co-occur with *HER2* (Figure S1C). We also noted that *HER3* mutations did not co-occur with *HER2* in-frame insertion mutations or when *HER2* was both mutated and amplified (Figures 1A and 1B). Intriguingly, in *HER2*-mutant breast cancers, co-occurring *HER3* mutations were mutually exclusive with co-occurring *PIK3CA*, suggesting that *HER3* and *PIK3CA* mutations are functionally redundant.

To identify the most common co-occurring *HER2* and *HER3* mutant allele pairs in breast cancer, we expanded our search

to include additional datasets from Foundation Medicine and cBioPortal. We identified 67 breast cancers harboring mutations in both genes (Table S1). The most common *HER2* mutations were L755S ($n = 24$), S310F/Y ($n = 16$), V777L ($n = 14$), and L869R/Q ($n = 7$). The most common *HER3* mutations were E928G ($n = 35$), V104L/M ($n = 8$), T355A/I ($n = 5$), and K329E/I ($n = 5$). These were similar to the most common single *HER2* and *HER3* missense mutations found in breast tumors (Figures S1D and S1E). The most common pairs are shown in Figure 1D. Since *HER3*^{E928G} is the most common co-mutated *HER3* allele, we focused our studies on that mutation paired with *HER2*^{L755S}, *HER2*^{V777L}, *HER2*^{L869R}, and *HER2*^{S310F}.

Co-occurring *HER2/HER3* mutants enhance KD dimerization and *HER2* kinase activation

To determine the mechanisms of activation of mutant *HER2* and *HER3*, we systematically evaluated the contributions of each mutation to *HER2* kinase activation and *HER2/HER3* dimerization (Figures S2A–S2C). Previous work demonstrated an increase in *HER2*^{WT} kinase activity when bound to *HER3*^{E928G} relative to *HER3*^{WT} (Collier et al., 2013). Subsequent work showed that *HER3*^{E928G} enhances EGFR/*HER3* dimerization affinity, potentially as a result of charge neutralization at the asymmetric dimer interface. However, neutralization of a glutamate interface residue in EGFR resulted in <2-fold increase in dimerization affinity, suggesting that charge neutralization may not be the primary contributor to *HER3*^{E928G} gain of function (Littlefield et al., 2014). Therefore, we probed the effects of *HER3*^{E928G} on *HER2/HER3* dimerization using a combination of Rosetta $\Delta\Delta G$ calculations and molecular dynamics (MD) simulations.

Consistent with previous studies, our Rosetta simulations suggest an enhanced dimerization affinity of *HER2*^{WT}/*HER3*^{E928G} relative to *HER2*^{WT}/*HER3*^{WT} (Figure 2A). Per-residue decomposition of Rosetta binding energy suggests that the largest contributions can be attributed to *HER2* L790 and *HER3* G927 (Figures 2B, S2D, and S2E). MD simulations displayed a reduced *HER2* L790–*HER3* G927 backbone hydrogen bond (H bond) distance (Figures 2C and 2D) and a ~1.3 kcal/mol increase in H bond stability in *HER2*^{WT}/*HER3*^{E928G} relative to *HER2*^{WT}/*HER3*^{WT} (Figures S2F and S2G). We failed to observe an increase in favorable contacts between charged interface residues (Figures 2B, 2D, S2D, and S2E). Our results suggest that the increased flexibility conferred to *HER3*^{E928G} at the dimerization interface by adjacent glycine residues (G927 and G928) increases dimerization affinity through backbone H bond optimization.

We next sought to understand the structural basis for potential synergy of *HER3*^{E928G} with the most common co-occurring *HER2* mutants in breast cancer (Figure 1D): L755S, V777L, and L869R. Previous studies have shown that *HER2* KD mutant monomers, including *HER2*^{V777L}, displayed enhanced kinase activity compared with the *HER2*^{WT} monomer; *HER2* activity was further increased by homodimerization of mutant *HER2* compared with the mutant monomer (Bose et al., 2013; Collier et al., 2013). Here, we investigated to what extent these mutations increase stability of the KD active conformation (Figure S2A) versus the stability of the asymmetric heterodimer interface (Figure S2B). We performed Rosetta $\Delta\Delta G$ calculations of *HER2* missense mutations in complex with *HER3*^{WT} or *HER3*^{E928G}

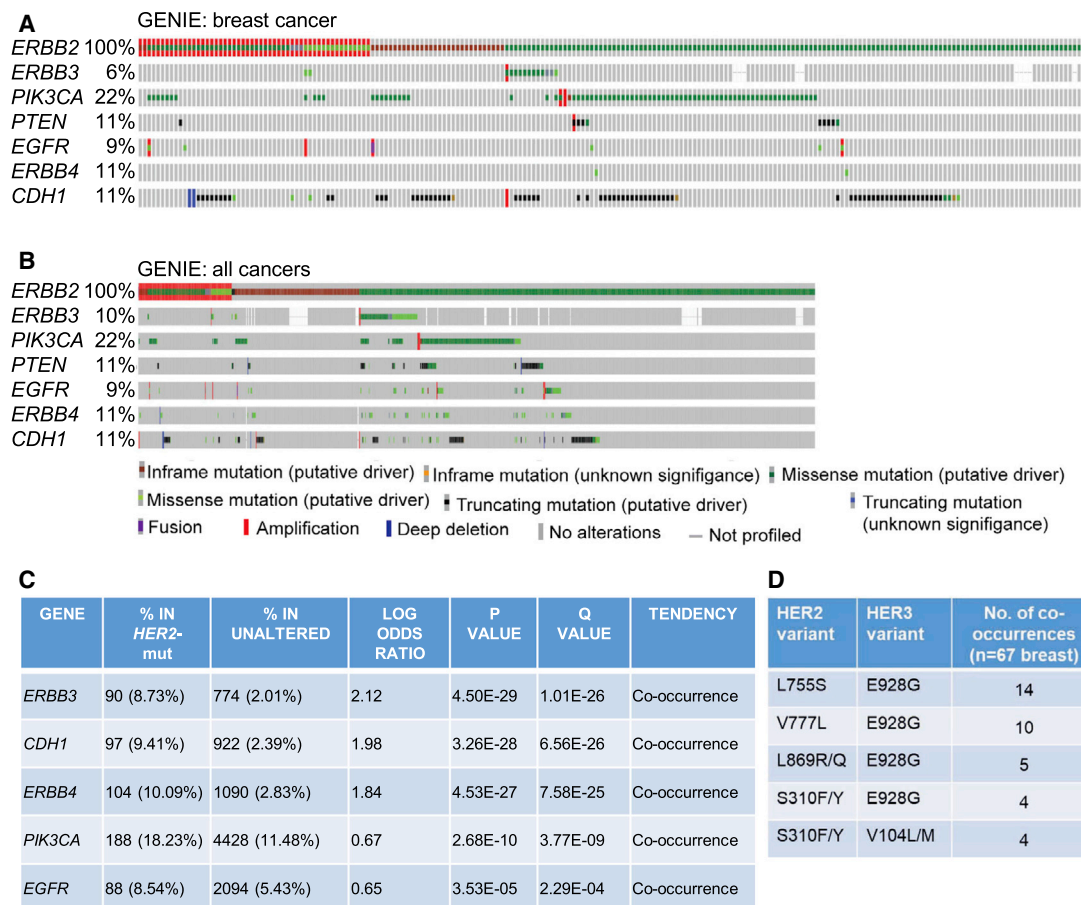


Figure 1. HER2 and HER3 mutations co-occur in breast and other cancers

(A and B) A total of (A) 277 HER2-mutant breast cancers and (B) 1,561 HER2-mutant pan-cancers in the Project GENIE database were interrogated for co-occurring alterations in the indicated genes. HER2 variants of unknown significance were excluded.

(C) Co-occurrence with HER2 mutations was analyzed using cBioPortal.

(D) The most common co-occurring HER2/HER3 mutations in breast cancer were determined using databases from Project GENIE, cBioPortal, and Foundation Medicine.

See also Figure S1.

(Figures S2B and S2C). The HER2 KD mutants did not increase dimerization affinity with HER3^{WT} (Figure 2A). In contrast, HER2^{S310F/Y} did increase dimerization affinity of the ECDs, potentially because the aromatic side chain of HER2 F/Y310 can make a stable hydrophobic contact with HER3 L272 (Figures S3A and S3B). HER3^{E928G} enhanced dimerization affinities over HER3^{WT} in all cases (Figures 2C and S3B).

We tested the hypothesis that HER2 missense mutants increase the stability of the KD active conformation using steered MD and umbrella sampling (US) simulations. We reasoned that mutations that reduce the energetic barrier to activation increase the propensity for dimer formation through conformational selection (Figures S2A and S2B). HER2^{WT} is more stable in the inactive conformation than the active conformation in our US simulations (Figures 2E and 2F). In contrast, both HER2^{L869R} and HER2^{L755S} favor the active conformation (Figures 2E and 2F). Consistent with previous accelerated MD simulations (Robichaux et al., 2019), HER2^{V777L} retained a preference for the inactive conformation in our simulations; however, the barrier to activation is

reduced, suggesting that HER2^{V777L} is more readily activated than HER2^{WT}. These results suggest that the tested HER2 KD missense mutations lower the free energy barrier between the inactive and active KD conformations, while HER3^{E928G} enhances the stability of the dimerization interface, such that HER2^{missense}/HER3^{E928G} co-mutations cooperatively promote oncogenic activation.

Co-occurring HER2/HER3 mutants enhance ligand-independent HER2/HER3 and PI3K activation

To test our computational predictions, we performed co-immunoprecipitation (co-IP) in HEK293 cells transiently transfected with WT (wild type) or mutant HER2 and HER3. In agreement with the structural predictions (Figures 2A and S3B), co-expression of HER3^{E928G} enhanced the interaction with HER2^{S310F}, L755S, or V777L compared with HER3^{WT} (Figures 3A and 3B). The stronger association between HER2^{L755S} and HER3^{E928G} compared with either mutant alone was confirmed by proximity ligation assay (PLA) (Figures S4A and S4B).

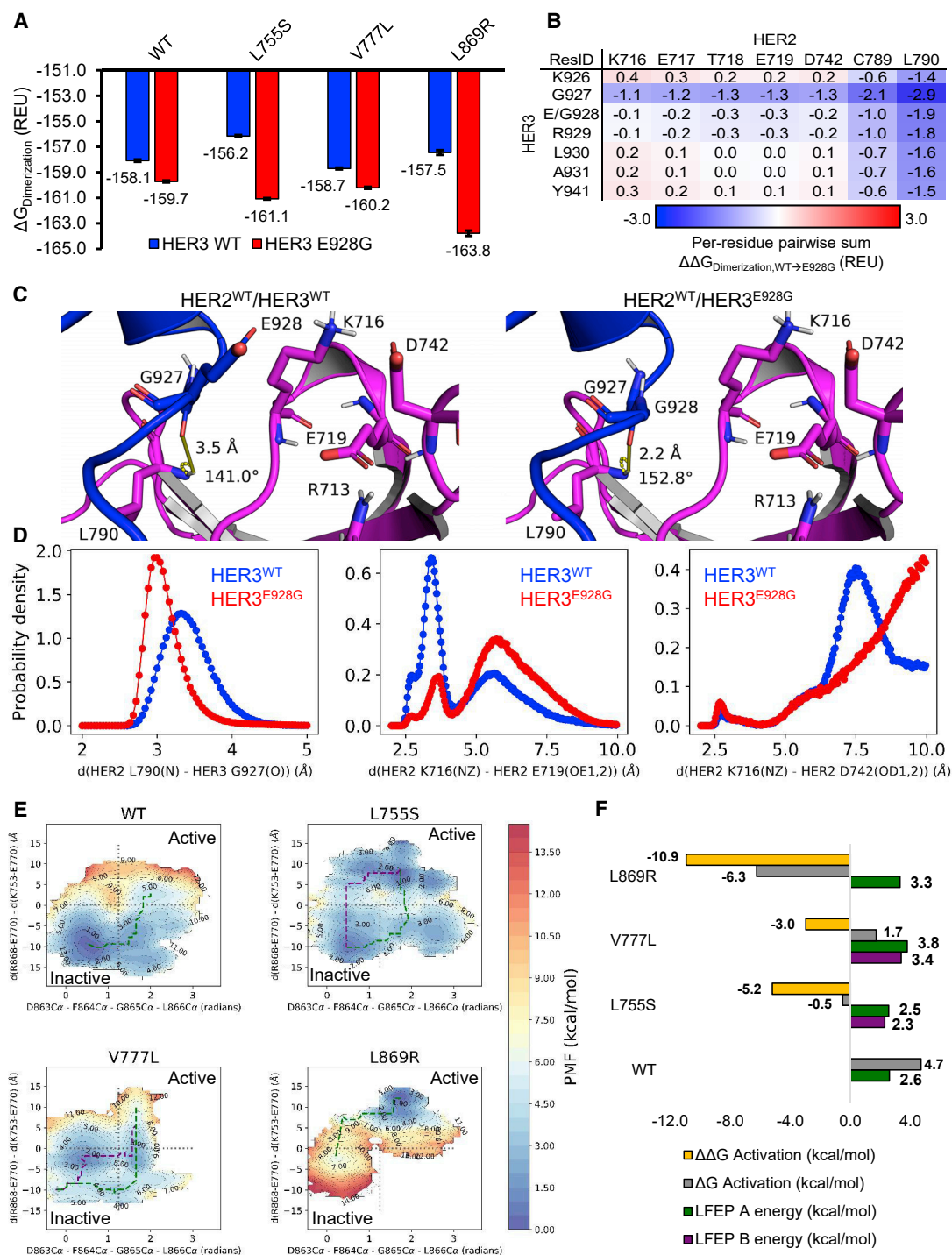


Figure 2. Co-occurring HER2/HER3 mutants enhance HER2/HER3 KD association and HER2 kinase activity

(A) Rosetta HER2/HER3 heterodimerization binding energy as mean \pm standard error across 20 lowest interface energy models.

(B) Pairwise sums of per-residue binding energy decomposition for HER2/HER3 heterodimerization.

(C) Comparison of the computational structural models of HER2^{WT}/HER3^{WT} and HER2^{WT}/HER3^{E928G} at the asymmetric dimer interface. HER2 is purple and HER3 is blue. The hydrogen bond distance and angle between G927-O/L790-NH and L790-N/L790-H/G927-O atoms, respectively, are depicted in yellow.

(D) Probability density plots of HER2^{WT}/HER3^{WT} and HER2^{WT}/HER3^{E928G} HER3 G927-O-HER2 L790-N hydrogen bond distance (left), HER2 K716-NZ-HER2 E719-OE1,2 bond distance (middle), and HER2 K716-NZ-HER2 D742-OD1,2 bond distance (right).

(legend continued on next page)

Treatment with the HER3 ligand neuregulin (NRG) triggers HER2/HER3 heterodimerization and pathway activation. We asked whether HER3^{E928G} can bypass the effect of NRG stimulation via enhanced interaction with the KD of HER2. Co-expression of HER3^{E928G} with HER2^{WT} strongly enhanced ligand-independent HER3 phosphorylation in serum-starved HEK293 cells (Figure 3C) in agreement with previous studies (Jaiswal et al., 2013). Similarly, HER2^{L755S} and HER2^{V777L}, when co-expressed with HER3^{WT}, increased ligand-independent HER2 and HER3 phosphorylation. Levels of P-HER3 were highest in the double-mutant cells. Similar results were obtained when only the intracellular domains of WT or mutant HER2 and HER3 were expressed (Figure S4C). Treatment with NRG was sufficient to stimulate HER2 and HER3 phosphorylation in cells co-expressing HER2^{WT} and HER3^{WT}, similar to the effects of HER2/HER3 double mutants in unstimulated cells (Figure 3C). These results support a model whereby the concurrent HER2/HER3 KD mutants promote ligand-independent HER2/HER3 KD association and HER2 kinase activation.

Next, we stably transduced MCF10A breast epithelial cells with WT and mutant *HER2*, each with WT or mutant *HER3*. In low-serum conditions, cells expressing the double mutants showed the highest levels of P-HER3 (Figure 3D). Unlike HER2, P-HER3 can directly bind to the p85 subunit of PI3K, inducing PI3K activity (Haikala and Janne, 2021). Consistent with this, levels of P-AKT were also highest in double-mutant cells (Figure 3D). P-HER3 and P-AKT were enhanced to a similar degree by NRG stimulation in HER2-mutant/HER3^{WT} cells (Figure S4D).

The above experiments were performed in the context of ectopic expression of *HER2* and *HER3*; however, most concurrent *HER2* and *HER3* mutations occur in the absence of *HER2* gene amplification (Figures 1A and 1B). Therefore, we expressed HER3^{WT} or HER3^{E928G} in (1) OVCAR8 ovarian cells, which contain an activating somatic HER2^{G776V} mutation without *HER2* amplification (Sudhan et al., 2020), and (2) MCF7 *HER2*-non-amplified breast cancer cells isogenically modified to express HER2^{L755S} or HER2^{V777L} at endogenous levels (Zabransky et al., 2015). Expression of HER3^{E928G} enhanced co-IP with mutant HER2 in OVCAR8 cells and enhanced P-HER3 in both models compared with HER3^{WT} (Figures 3E and S4E). Levels of P-AKT were also increased in OVCAR8 cells expressing HER3^{E928G}, but not in MCF7 double-mutant cells, perhaps because these cells harbor an activating *PIK3CA* mutation. These results suggest that concurrent HER2/HER3 mutants enhance ligand-independent PI3K activity, providing a plausible explanation for the mutual exclusivity of co-occurring *HER3* and *PIK3CA* mutations in *HER2*-mutant breast cancers (Figure 1A).

We noted above that *HER2* insertion mutations did not co-occur with *HER3* mutations (Figures 1A and 1B). Therefore, we asked whether the HER2^{Y772_A775dup} (HER2^{YVMA}) insertion mutant could activate HER2/PI3K to a similar degree as co-occurring HER2 and HER3 missense mutants. We modeled the insertion mutants HER2^{YVMA} and HER2^{G778_P780dup} (HER2^{GSP}) mutations based on the HER2^{WT} and EGFR^{D770_N771insNPG} struc-

tures (Figure S4F). Simulations suggest that HER2^{GSP} and HER2^{YVMA} have reduced free energy barriers to activation relative to HER2^{WT} (Figures S4F and S4G). Next, we stably transduced MCF10A cells with HER2^{YVMA} and HER3^{WT} or HER3^{E928G}. Both HER2/HER3 co-IP and P-AKT levels were similar in cells expressing HER2^{YVMA}/HER3^{WT} and HER2^{L755S}/HER3^{E928G} (Figures 3F and S4H). Co-expression of HER3^{E928G} with HER2^{YVMA} did not further increase P-AKT, suggesting that *HER2* insertion mutations and *HER3* mutations are stronger activators of PI3K than *HER2* missense mutations alone.

While HER3^{E928G} is the most common *HER3* mutation in breast cancer, we noted several cases of co-occurring *HER2*/*HER3* ECD mutations (Figure 1D; Table S1). Thus, we expressed each *HER3* ECD mutation together with HER2^{WT} or HER2^{S310F} in HEK293 cells. HER2^{S310F} expression with HER3^{WT} resulted in increased ligand-independent HER2 and HER3 phosphorylation compared with HER2^{WT} (Figure S4I). However, co-expression of *HER3* ECD mutants did not further enhance phospho-HER2 or -HER3, suggesting that these *HER3* mutants do not promote ligand-independent HER2/HER3 activation.

Co-occurring HER2/HER3 mutants enhance oncogenic growth and invasion

Next, we asked whether concurrent HER2/HER3 mutants cooperate to transform breast cancer cells. While most of the co-occurring mutations enhanced growth in 2D and 3D (Figures 4A and 4B), expression of the most common pair, HER2^{L755S}/HER3^{E928G}, did not further enhance monolayer 2D growth above that of HER2^{L755S} alone. However, when cultured in 3D Matrigel, MCF10A HER2^{L755S}/HER3^{E928G} cells formed large invasive acini in the absence of added NRG1 (Figures 4C and 4D), suggestive of a more transformed phenotype. Similar invasive acini were formed by cells expressing HER2^{S310F}/HER3^{E928G} and HER2^{L869R}/HER3^{E928G}, but not by cells expressing either HER2 variant with HER3^{WT} (Figure S5A). Notably, NRG1 treatment phenocopied the effect of HER3^{E928G} in cells expressing HER3^{WT} and HER2 mutants (Figure 4C). Ligand-independent invasive acini were formed by cells transduced with HER2^{YVMA}, but this effect was not enhanced by co-transduction with mutant *HER3*. Invasion through Matrigel-coated chambers was strongly enhanced by all of the double mutants or by HER2^{YVMA}/HER3^{WT} (Figures 4E, 4F, and S5B–S5E). Together, these results suggest that concurrent HER2/HER3 mutants enhance ligand-independent PI3K pathway activation, which is associated with increased invasion (Samuels et al., 2005).

HER3^{E928G} promotes resistance to HER2-targeting antibodies

We next asked whether HER2- and HER3-targeting antibodies could disrupt the association of HER3^{E928G} with HER2 and the enhanced oncogenicity conferred by co-occurring *HER2*/*HER3* mutations. We used the HER2 antibodies trastuzumab and pertuzumab, which disrupt ligand-dependent and -independent HER2/HER3 dimers (Agus et al., 2002; Junttila et al., 2009) and

(E) Activation state conformational free energy landscape of HER2^{WT} and mutants (see the STAR Methods).

(F) Quantification of free energy difference between active and inactive states (gray), relative free energy difference compared with HER2^{WT} (yellow), and integration along the lowest free energy path(s) (green and purple).

See also Figures S2 and S3.

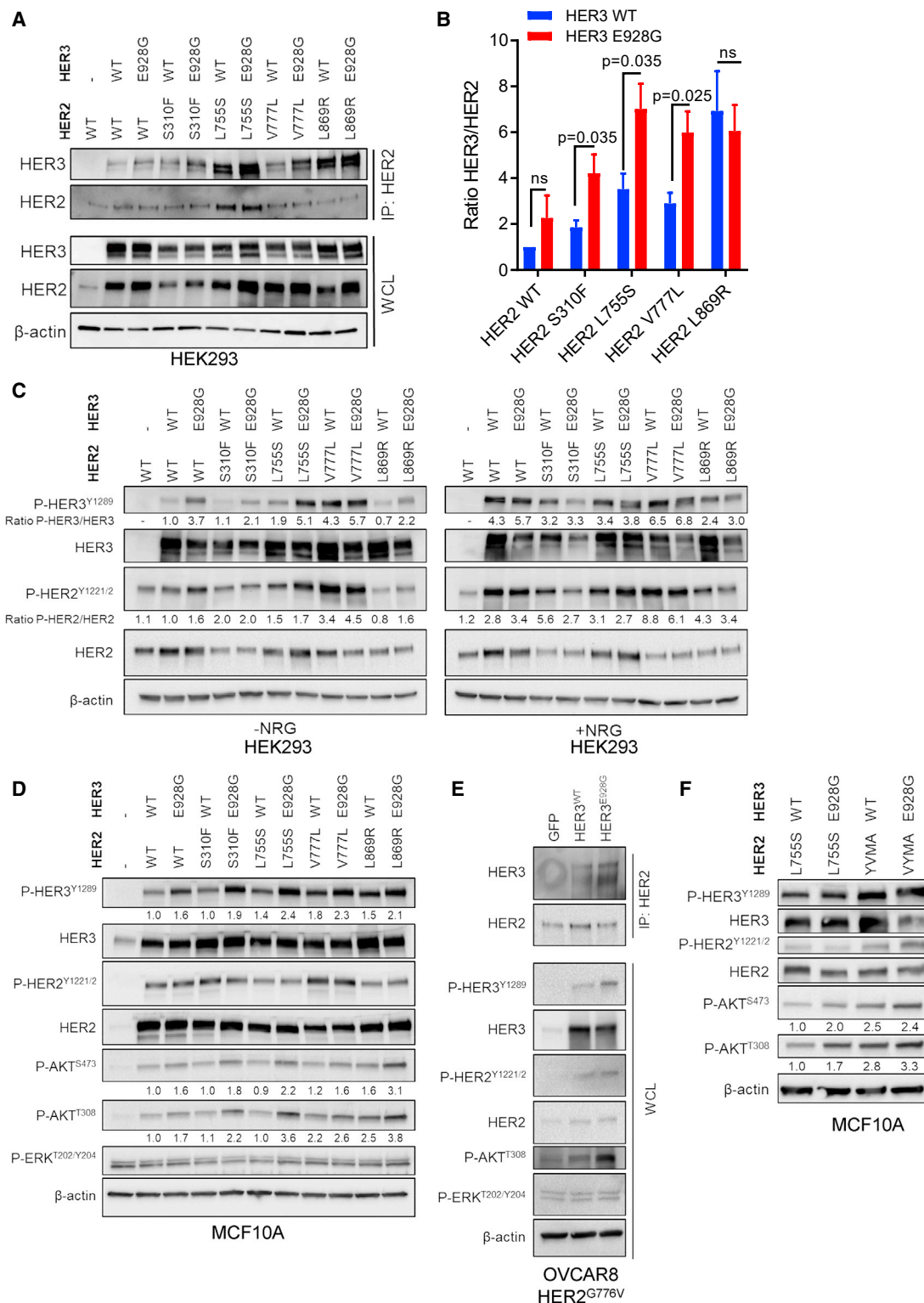


Figure 3. HER3^{E928G} enhances HER2/HER3 association and PI3K pathway activation

(A) HEK293 cells were co-transfected with the indicated transgenes. HER2 IP was performed as in the [STAR Methods](#).

(B) Immunoblot bands from four independent HER2 IP experiments in HEK293 cells were quantified using ImageJ. Data represent the mean \pm SEM (n = 4). p values, Student's t test.

(legend continued on next page)

PanHER, a mixture of antibodies targeting EGFR, HER2, and HER3 that induces ERBB receptor downregulation (Jacobsen et al., 2015). In agreement with previous studies (Greulich et al., 2012; Kavuri et al., 2015), MCF10A cells expressing the extracellular HER2^{S310F} mutation were exquisitely sensitive to the combination of trastuzumab and pertuzumab and to PanHER (Figures 5A–5C and S6A). However, co-expression of HER3^{E928G} reversed this response (Figures 5B and 5C). co-IP of cell lysates with HER2 antibodies showed that HER2^{S310F}/HER3^{WT} dimerization was disrupted by trastuzumab and pertuzumab. In cells expressing HER2^{S310F}/HER3^{E928G}, dimerization was not affected by antibody treatment (Figure 5D). Similarly, the antibodies blocked P-HER3, P-AKT, and the downstream effector P-S6 in MCF10A cells expressing HER2^{S310F}/HER3^{WT}, but failed to do so in cells expressing HER2^{S310F}/HER3^{E928G} (Figure 5E). Flow cytometry analysis revealed that HER3^{E928G} did not disrupt trastuzumab binding to cell surface HER2 (Figure S6B). These results suggest that HER3^{E928G} may enable the intracellular association of HER2 and HER3 KD mutants, even when the ECD interaction is disrupted by neutralizing antibodies.

HER3^{E928G} modulates sensitivity to neratinib

The HER2 TKI neratinib has emerged as a promising treatment for HER2-mutant metastatic breast cancer. However, only a subset of HER2-mutant patients respond to neratinib (Hyman et al., 2018; Ma et al., 2017; Smyth et al., 2020). Therefore, we asked whether concurrent HER3^{E928G} mutations affect the ability of neratinib to inhibit HER2. Neratinib is an ATP-competitive TKI, so its efficacy is a function of ATP-binding affinity. MD simulations and molecular mechanics generalized Born and surface area binding energy calculations of the HER2^{WT}-ATP complex heterodimerized with HER3^{WT} or HER3^{E928G} suggest that HER3^{E928G} enhanced binding affinity to ATP (Figure 6A). Similar results were seen in simulations of missense variants (Figures 6B and 6C). Our simulations suggest that HER3^{E928G} reduces the binding affinity of neratinib to HER2^{WT}, HER2^{L755S}, and HER2^{L869R} (Figure 6D). They also suggest that HER2^{L755S}, and to a lesser extent HER2^{L869R}, may have reduced sensitivity to neratinib that is compounded by co-occurrence with HER3^{E928G}, consistent with previous reports that HER2^{L755S} may be less sensitive to HER2 TKIs (Li et al., 2019; Robichaux et al., 2019). In contrast, HER2^{V777L} is expected to mostly retain sensitivity to neratinib even when co-occurring with HER3^{E928G} (Figure 6D).

We subsequently tested the neratinib sensitivity of MCF10A cells co-expressing WT or mutant HER2 and HER3. Co-expression of HER3^{E928G} resulted in a ~15-fold shift in neratinib half-maximal inhibitory concentration (IC₅₀) in MCF10A HER2^{S310F}-expressing cells (Figure 6E). Similar results were obtained with other HER2 TKIs (poziotinib, afatinib, and tucatinib), suggesting that expression of HER3^{E928G} reduces sensitivity to most HER2 ATP-competitive inhibitors (Figure S7A). However, the shift in IC₅₀ varied in a HER2 allele-specific manner (Figures 6F and

S7B), consistent with our computational predictions (Figures 6D; Table S2). For example, HER2^{L755S} cells were less sensitive to neratinib compared with HER2^{S310F}, consistent with previous reports (Li et al., 2019; Nagano et al., 2018; Robichaux et al., 2019). This trend was similar in 3D Matrigel cultures: treatment with neratinib blocked growth of MCF10A HER2^{S310F}/HER3^{WT} and HER2^{V777L}/HER3^{WT} cells and partially blocked growth of MCF10A HER2^{L869R}/HER3^{WT} cells, whereas cells expressing HER2^{L755S} were largely resistant (Figure 6G). Co-expression of HER3^{E928G} reduced the response to neratinib in cells expressing most HER2 mutants. Consistent with the effects on cell growth, neratinib treatment blocked P-HER3, P-AKT, and P-S6 in MCF10A cells expressing HER2^{mutant}/HER3^{WT}, but to a lesser degree in cells expressing HER2^{L755S}/HER3^{WT}, while neratinib failed to block HER3/PI3K signaling in cells expressing HER3^{E928G} (Figure S7C). Furthermore, OVCAR8 cells (somatic HER2^{G776V}) ectopically expressing HER3^{E928G} (Figure 3E) exhibited reduced sensitivity to neratinib compared with cells expressing HER3^{WT} (Figure S7D).

Next, we established organoids from an HER2-mutant, non-amplified breast tumor model: the SA493 patient-derived xenograft (PDX), derived from an ER+/HER2^{S310F} lobular breast cancer (Eirew et al., 2015). We confirmed that the organoids retained the HER2^{S310F} mutation (Figure S7E). Next, we stably transduced these organoids with HER3^{WT} or HER3^{E928G} (Figure S7F); expression of HER3^{E928G} in these HER2-mutant organoids increased P-HER3, P-AKT, and P-S6 (Figure S7G). In ligand-free media, cells expressing HER3^{E928G} formed larger, less-organized organoids compared with those expressing HER3^{WT}, suggesting that HER3^{E928G} promotes a more aggressive phenotype of this HER2-mutant breast cancer model (Figure S7H). While parental organoids and those expressing HER3^{WT} were quite sensitive to trastuzumab + pertuzumab, neratinib, or the combination, organoids expressing HER3^{E928G} exhibited markedly reduced sensitivity to these agents (Figure 6H). Together, our results suggest that HER3^{E928G} increases ligand-independent growth and reduces sensitivity to HER2-targeting agents in multiple HER2-mutant tumor models.

Cancer cells with co-occurring HER2/HER3 mutations are sensitive to combined inhibition of HER2 and PI3Kα

Our results suggest that HER2/HER3 co-mutations hyperactivate the PI3K/AKT pathway and result in relative resistance to HER2-targeted therapies. Therefore, we tested the combination of neratinib with a PI3K inhibitor in MCF10A cells expressing the double mutants. The combination of neratinib with the PI3Kα inhibitor alpelisib or with the pan-PI3K inhibitor buparlisib blocked P-AKT and P-S6 in MCF10A HER2^{L755S}/HER3^{E928G} and HER2^{YVMA} cells more potently than either drug alone (Figure 7A). The combination of neratinib and alpelisib also strongly reduced colony growth and invasive acini formation in 3D Matrigel by these

(C) HEK293 cells were co-transfected with the indicated transgenes, serum-starved overnight, then stimulated ±10 ng/mL NRG1 for 10 min.

(D) MCF10A cells stably expressing the indicated transgenes or GFP control (–/–) were incubated in EGF/insulin-free media +1% CSS overnight.

(E) OVCAR8 cells stably expressing pLX302-GFP (control), HER3^{WT}, or HER3^{E928G} were incubated in RPMI +1% CSS overnight, then subjected to HER2 IP.

(F) MCF10A cells stably expressing the indicated transgenes were incubated and lysed as in (D). Where indicated, numbers below bands represent quantification of band intensity by ImageJ; ratios were normalized to WT/WT.

See also Figure S4.

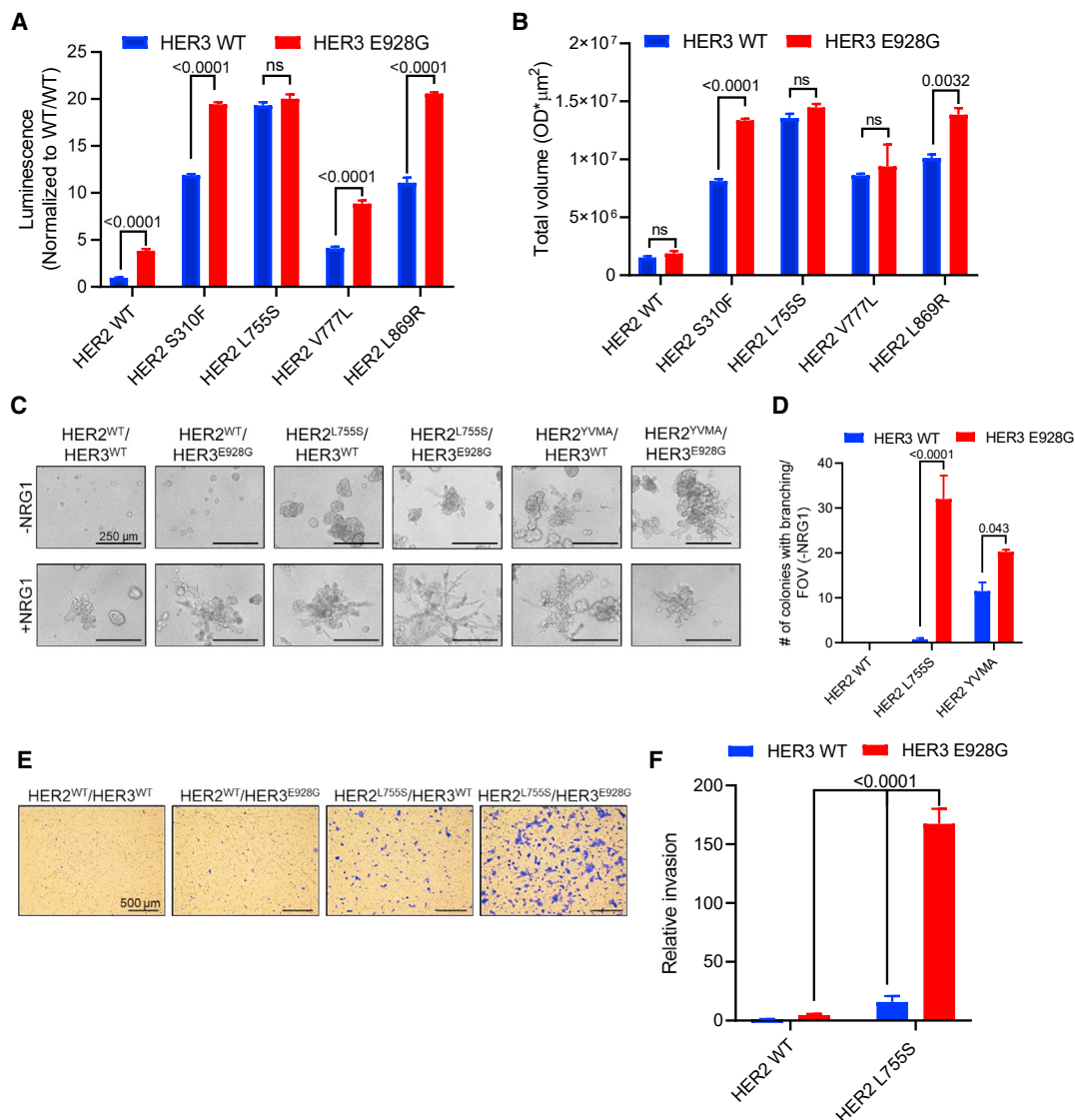


Figure 4. Co-occurring HER2/HER3 mutations enhance oncogenic growth and invasion of breast epithelial cells

(A) MCF10A cells stably expressing the indicated transgenes were grown in 2D in EGF/insulin-free medium +1% CSS. After 6 days, cell viability was measured by CellTiter-Glo. Data represent the mean \pm SEM (n = 4). p values, two-way ANOVA + Bonferroni.

(B) MCF10A cells were grown in 3D Matrigel in EGF/insulin-free medium +1% CSS and stained with 3-(4,5-dimethylthiazol-2-yl)-2,5-diphenyltetrazolium bromide (MTT). The total volume of colonies per well was quantified using the GelCount instrument. Data represent the mean \pm SEM (n = 3). p values, two-way ANOVA + Bonferroni.

(C) MCF10A cells stably expressing the indicated transgenes were grown in 3D Matrigel in EGF-free medium +1% CSS \pm 10 ng/mL NRG1 for 7 days. Scale bars, 250 μm .

(D) The number of colonies showing invasive branching per field of view (FOV) from (C) was quantified. Data represent the mean \pm SEM (n = 3). p values, two-way ANOVA + Bonferroni.

(E) MCF10A cells stably expressing the indicated genes were seeded on Matrigel-coated chambers. After 22 h, invading cells were stained with crystal violet. Scale bars, 500 μm .

(F) Relative invasion (normalized to WT/WT) from two FOVs per well was quantified in ImageJ. Data represent the mean \pm SEM (n \geq 3). p values, two-way ANOVA + Bonferroni.

See also Figure S5.

cells (Figures 7B and 7C). Next, we examined CW2 colorectal cancer cells, which harbor somatic HER2^{L755S}/HER3^{E928G} mutations (Figure S8A) (Kloth et al., 2016). Small interfering RNA (siRNA)-induced knockdown of either HER2^{L755S} or HER3 showed that the proliferation and PI3K activity in these cells is

partially dependent on both mutant HER2 and HER3 (Figures S8B–S8F). The combination of neratinib and alpelisib was required to eliminate P-AKT and synergistically blocked proliferation in these cells (combination index = 0.42) (Figures 7D and 7E). While 4 h treatment with neratinib + alpelisib strongly

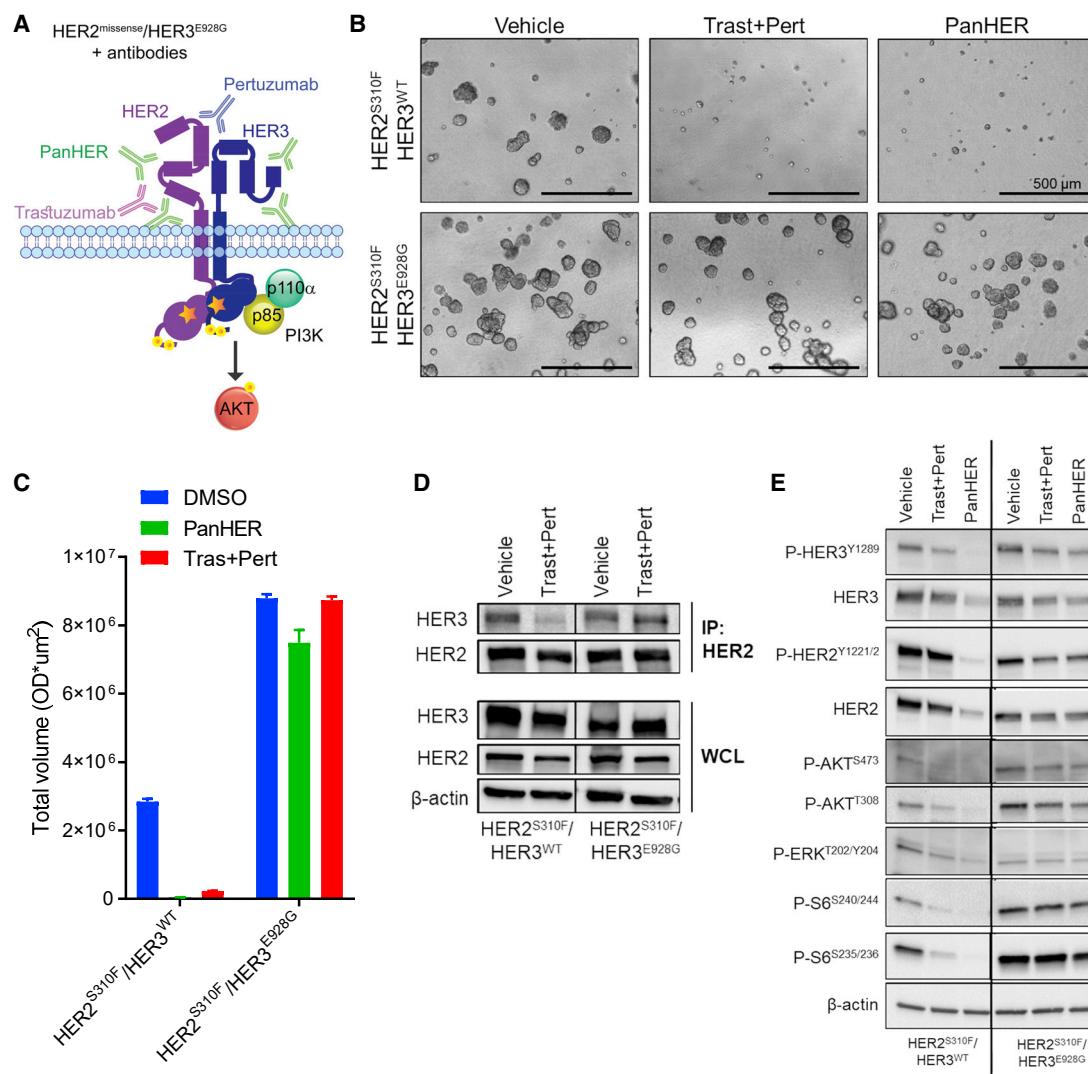


Figure 5. HER3^{E928G} promotes resistance to HER2- and HER3-targeting antibodies by retaining HER2/HER3 KD association

(A) Model of HER2/HER3^{E928G} heterodimer bound to trastuzumab, pertuzumab, or PanHER.

(B) MCF10A cells stably expressing the indicated genes were grown in 3D Matrigel in EGF/insulin-free medium +1% CSS and treated with vehicle (PBS), 20 μ g/mL PanHER, 20 μ g/mL each trastuzumab + pertuzumab for 7 days. Scale bars, 500 μ m.

(C) The total volume of colonies per well was quantified using the GelCount instrument. Data represent the mean \pm SEM (n = 3).

(D) MCF10A cells stably expressing the indicated transgenes were treated with vehicle (PBS), 20 μ g/mL each trastuzumab and pertuzumab for 24 h in EGF/insulin-free medium +1% CSS. Following an acid wash to remove bound antibodies, HER2 IP was performed. Line denotes removal of irrelevant lanes; blots are from the same gel/blot.

(E) MCF10A cells stably expressing the indicated transgenes were treated with vehicle (PBS), 20 μ g/mL each trastuzumab and pertuzumab, or 20 μ g/mL PanHER for 24 h in EGF/insulin-free medium + 1% CSS. Line denotes removal of irrelevant lanes; blots are from the same gel/blot.

See also Figure S6.

blocked P-ERK and P-S6 in CW2 and MCF10A HER2^{L755S}/HER3^{E928G} cells, a rebound was seen at 24 h of treatment (Figures S8G and S8H), perhaps reflecting activation of feedback pathways (Chakrabarty et al., 2012; Chandralapathy et al., 2011). In addition, the combination delayed growth of CW2 xenografts more potently than each drug alone (Figures 7F and S8I). Together, our data suggest that addition of a PI3K α inhibitor increases the sensitivity of tumors with HER2^{mut}/HER3^{E928G} to HER2 TKIs.

DISCUSSION

Somatic HER2 mutations are increasingly being recognized as targetable alterations in breast and other cancers (Cocco et al., 2019; Mishra et al., 2017), prompting a number of studies testing HER2 TKIs in HER2-mutant cancers (Hyman et al., 2018; Robichaux et al., 2019; Smyth et al., 2020). Here, we investigated the intriguing co-occurrence of mutations in HER2 and HER3, genes that encode members of the same signaling complex. We

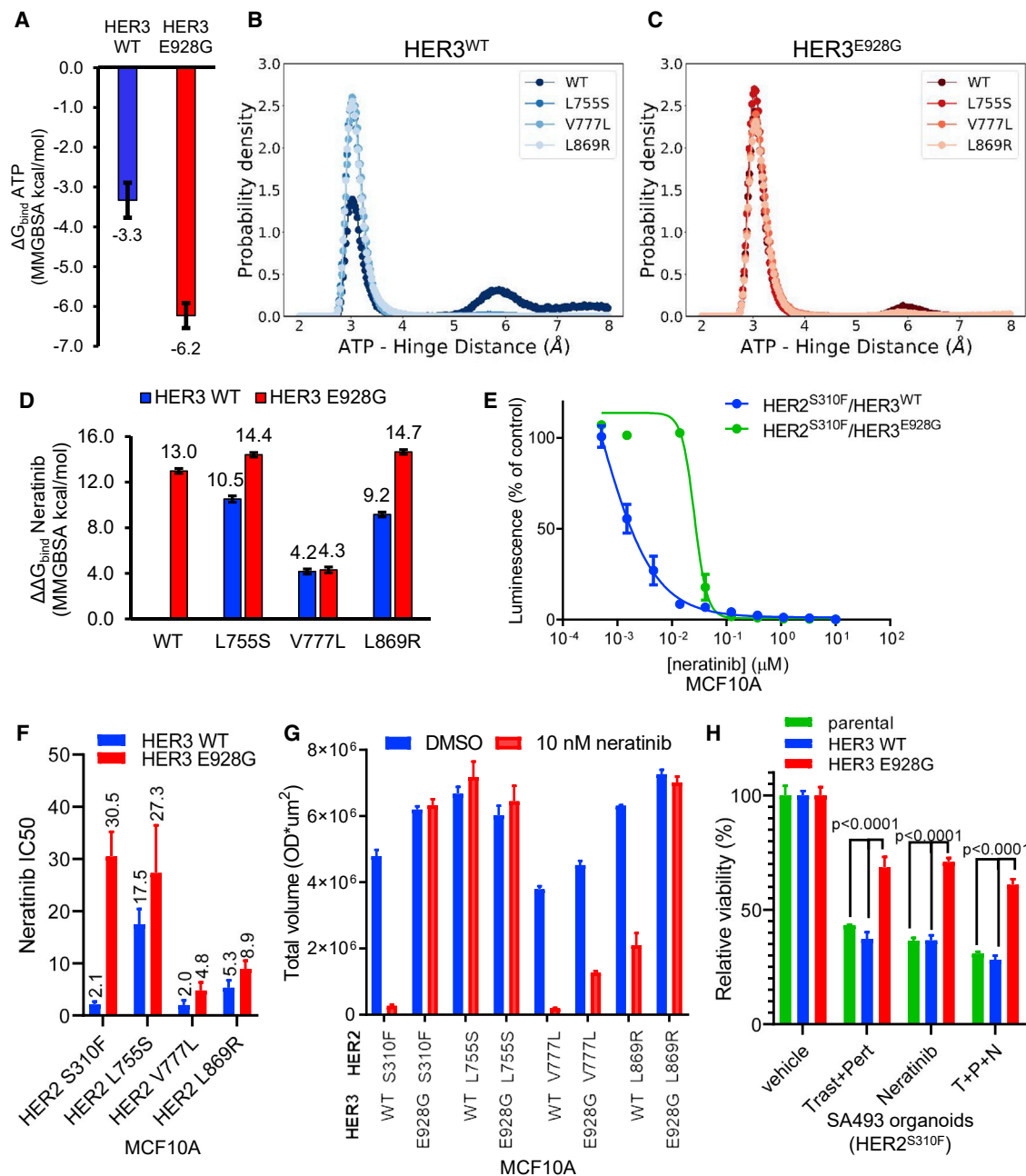


Figure 6. Co-occurring *HER3* mutations modulate neratinib sensitivity in *HER2*-mutant cells

(A) Molecular mechanics generalized Born and surface area (MM-GBSA) binding affinity estimates of ATP to *HER2*^{WT}/*HER3*^{WT} and *HER2*^{WT}/*HER3*^{E928G}. (B and C) (B) Probability density hinge-ATP H bond distance in *HER2* WT, L755S, V777L, and L869R dimerized with *HER3*^{WT} or (C) *HER3*^{E928G}. (D) MM-GBSA relative binding affinity estimates of neratinib to *HER2* variants heterodimerized with *HER3*^{WT} or *HER3*^{E928G}. Estimates are reported as mean \pm standard error across three independent trajectory samples. (E) MCF10A *HER2*^{S310F}/*HER3*^{E928G} cells were grown in EGF/insulin-free medium + 1% CSS and treated with the indicated concentrations of neratinib for 6 days. Cell viability was measured using CellTiter-Glo. (F) Neratinib IC₅₀ values were determined as in (E). Data represent the mean of three independent dose-response curves containing four replicates each. (G) MCF10A cells stably expressing the indicated transgenes were grown in 3D Matrigel in EGF-free medium + 1% CSS \pm 10 nM neratinib and stained with MTT. Data represent the mean \pm SEM (n = 3). (H) SA493 (*HER2*^{S310F}) breast cancer organoids stably expressing *HER3*^{WT}, *HER3*^{E928G}, or untransduced (parental) were treated with 20 μ g/mL each trastuzumab (T) and pertuzumab (P), 10 nM neratinib (N), or the combination. Viability was assessed 6 days later using the 3D CellTiter-Glo assay and normalized to vehicle-treated controls. Bars represent the mean \pm SEM (n = 4). p value, two-way ANOVA + Bonferroni. See also Figure S7.

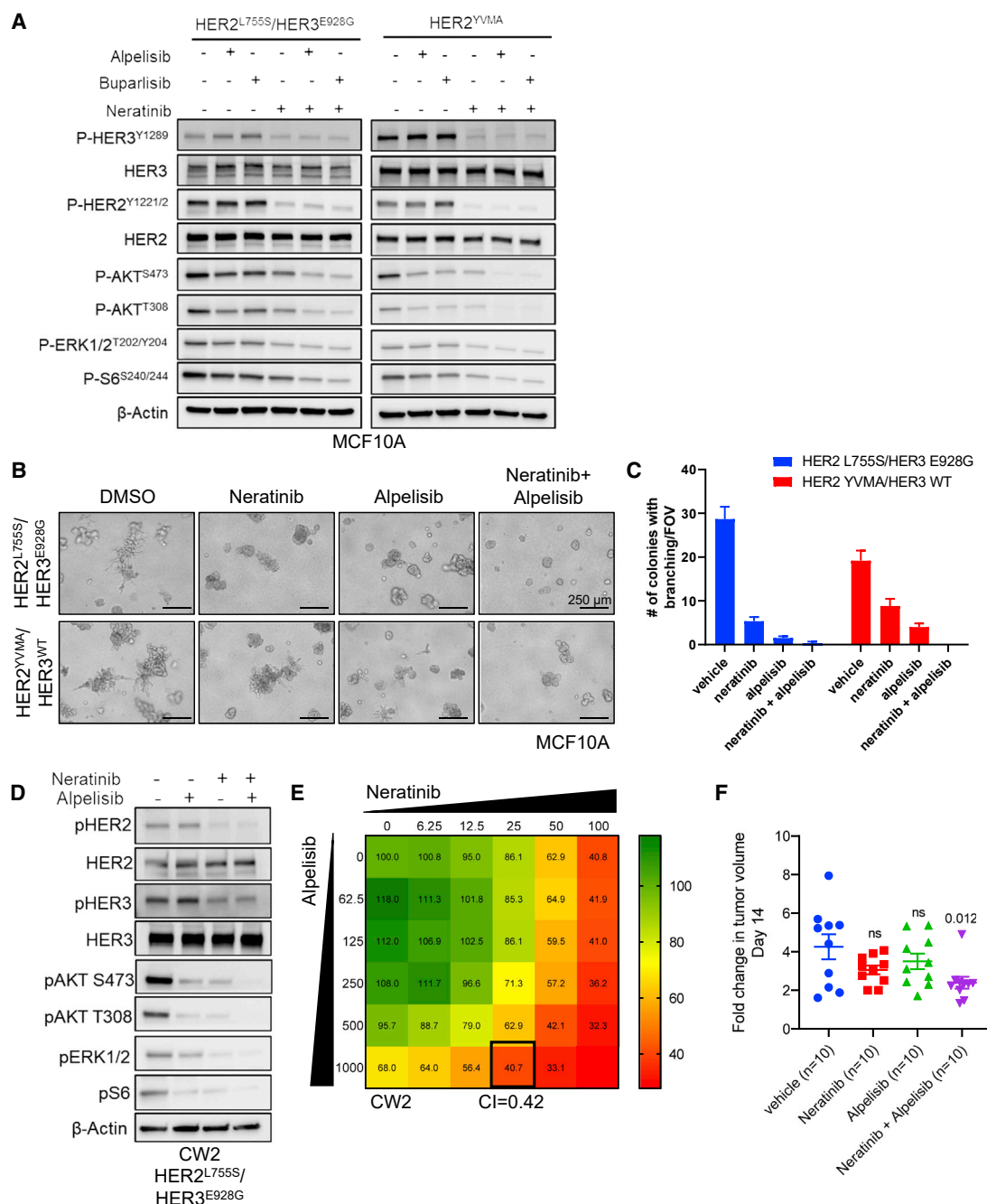


Figure 7. Cancer cells harboring co-occurring mutations in *HER2* and *HER3* are sensitive to combined inhibition of *HER2* and *PI3Kα*

(A) MCF10A cells stably expressing the indicated transgenes were treated with vehicle (DMSO), 500 nM alpelisib, 500 nM buparlisib, 50 nM neratinib, or the indicated combinations for 4 h in EGF/insulin-free medium + 1% CSS.

(B) MCF10A cells stably expressing the indicated genes were grown in 3D Matrigel in EGF/insulin-free medium + 1% CSS treated with vehicle (DMSO), 20 nM neratinib, 1 μM alpelisib, or the combination. Scale bars, 250 μm.

(C) The number of colonies showing invasive branching per field of view (FOV) from (B) was quantified. Data represent the average ±SD (n = 3).

(D) CW2 colon cancer cells were treated with vehicle (DMSO), 500 nM alpelisib, 50 nM neratinib, or the combination in serum-free medium for 4 h. Lysates were probed with the indicated antibodies.

(E) CW2 cells were treated with increasing concentrations of neratinib (0–100 nM) or alpelisib (0–1,000 nM) alone or in combination for 72 h. Cell viability was quantified using the CyQuant assay and combination indices were determined using the Chou-Talalay test. Numbers inside each box represent the average percent viability relative to untreated controls from two independent experiments.

(F) Mice carrying CW2 xenografts were treated with vehicle, 40 mg/kg neratinib, 40 mg/kg alpelisib, or the combination for 14 days, starting when tumors reached ~200 mm³. p values (relative to vehicle), one-way ANOVA + Bonferroni.

See also Figure S8.

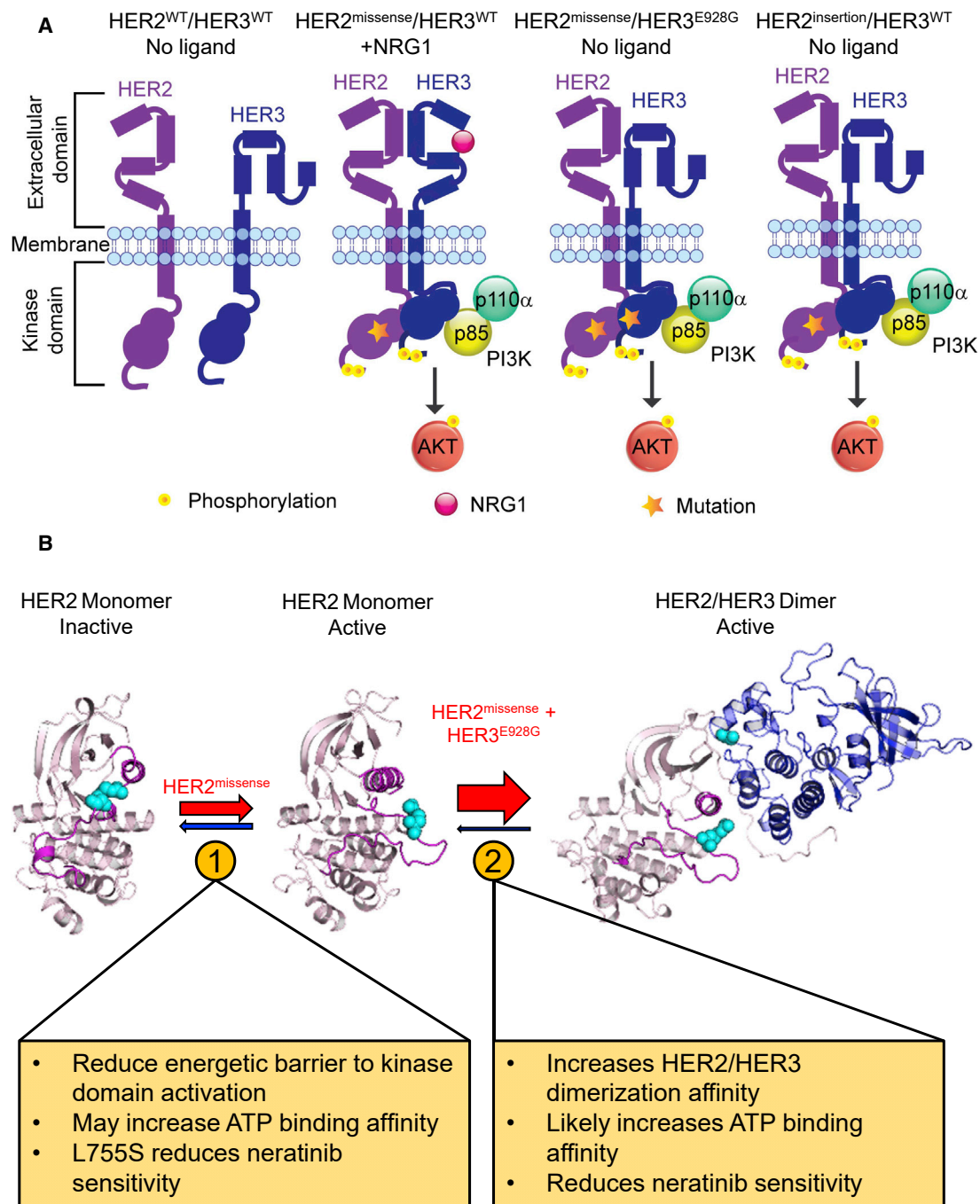


Figure 8. Model of HER2/PI3K pathway activation by co-occurring HER2/HER3 mutations

(A) In the absence of ligand, WT HER3 is in the closed conformation and does not interact with WT HER2. NRG1 treatment promotes HER2/HER3 heterodimerization and a HER2 missense mutation further increases HER3 phosphorylation to recruit the p85 subunit of PI3K and activates PI3K signaling. In the absence of ligand, the HER3^{E928G} mutation phenocopies NRG1 treatment by increasing HER2/HER3 association via enhanced binding of the HER2/HER3 KDs leading to constitutive activation of PI3K. HER2 insertion mutations alone also increase ligand-independent HER2/HER3 association and PI3K activation.

(B) Proposed conformational selection model showing how HER2^{missense} mutations cooperate with HER3^{E928G} to enhance receptor heterodimerization and HER2 kinase activation.

reasoned that such patterns of co-occurrence indicate a selective advantage conferred by both oncogenes during tumor evolution. Recent studies have found that a number of oncogenes, including

HER2, HER3, and PIK3CA, often harbor more than one mutation in the driver oncogene, termed “composite mutations” (Gorelick et al., 2020; Saito et al., 2020). In particular, composite PIK3CA

mutations have been shown to increase PI3K activity and PI3K-dependent tumor growth (Vasan et al., 2019). We speculate that single gain-of-function missense mutations may not fully maximize HER2/HER3 activation, such that either composite *HER2* mutations, or co-occurring *HER2/HER3* mutations, increase pathway activation and provide a selective advantage.

It is well established that HER2-driven transformation, invasion, and metastasis depends on HER3/PI3K signaling (Holbro et al., 2003; Smirnova et al., 2012; Xue et al., 2006). In addition, activating mutations *PIK3CA* cooperate with amplified WT HER2, enhancing invasion and metastasis (Chakrabarty et al., 2010; Hanker et al., 2013). In line with these data, co-mutant HER2/HER3 hyperactivate PI3K/AKT and enhance transformation/invasion (Figures 3 and 4), potentially explaining the observed mutual exclusivity of these alterations in *HER2*-mutant breast tumors (Figure 1A). While clinical information of patients with co-occurring *HER2/HER3* mutations is scarce, future studies should address whether this genomic subset of patients correlates with increased metastasis.

We observed strong concordance between our computational structural predictions and biological results (Table S2). Our simulations suggest that co-occurring HER2 and HER3 mutants enhance the coupling of the receptor KDs, such that HER2 missense mutants increase kinase conformational activation relative to HER2^{WT}, while HER3^{E928G} enhances heterodimerization affinity (Figure 8B). This model is supported by co-IP, PLA, and immunoblot assays (Figures 3 and S4). Our simulations also predicted that HER2^{L755S} binds neratinib with reduced affinity (Figure 6D). Indeed, HER2^{L755S} was less sensitive to neratinib than the other HER2 mutants in our cell viability and 3D Matrigel assays (Figures 6F, 6G, S7B, and S7C), consistent with previous reports (Li et al., 2019; Robichaux et al., 2019). Likewise, our computational modeling predicted that neratinib binding depends on the specific *HER2* mutation within the HER2/HER3^{E928G} heterodimer (Figure 6D). This was confirmed in cell-based assays: while HER3^{E928G} strongly reduced neratinib sensitivity and neratinib binding in the absence of HER2 KD mutations (i.e., HER2^{S310F}/HER3^{E928G}), the HER2^{V777L}/HER3^{E928G} double mutant retained a strong interaction with neratinib and a high degree of sensitivity to neratinib (Figures 6F and 6G). Thus, HER3^{E928G} reduces sensitivity to neratinib in a HER2 allele-specific manner.

Our results suggest that *HER2* allele-specific differences in neratinib sensitivity are related to unique mechanisms of activation of each mutant. We hypothesize that HER2^{L755S} stabilizes the N-terminal region of the α C helix (Figures S3C and S3D). In contrast, we hypothesize that HER2^{V777L} increases hydrophobic contacts in the back hydrophobic pocket, but may also function similar to KD insertion mutants (Figures S3E and S3F). Because L755S more rigidly pulls the α C helix inward from the N-terminal region, the force applied perpendicularly to the α C helix by the neratinib pyridine ring may be greater than in V777L, analogous to EGFR^{L858R} (Sogabe et al., 2012). Finally, we hypothesize that HER2^{L858R} decreases the stability of the KD inactive conformation. The intermediate neratinib sensitivity of HER2^{L858R} may be the result of increased occupancy of the active conformation without direct stabilization of the α C helix (Figures S3G and S3H). Crystallographic studies coupled with detailed structure-activity relationship profiling and long-timescale MD simulations are needed to fully elucidate the structural basis of TKI sensitivity/resistance.

In recent clinical trials of neratinib in patients with *HER2*-mutant cancer, patients with concurrent *HER3* mutations in their tumors exhibited a lower clinical response and shorter progression-free survival (Hyman et al., 2018; Smyth et al., 2020). Our results provide evidence that HER3^{E928G} confers reduced sensitivity to neratinib in *HER2*-mutant breast cancer cells. In addition to reducing neratinib sensitivity, we found that expression of HER3^{E928G} strongly promoted resistance to HER2- and HER3-targeting antibodies (trastuzumab + pertuzumab or PanHER; Figure 6B). Similarly, Jaiswal et al. (2013) found that HER3^{E928G} was insensitive to HER2- and HER3-targeting antibodies. We predict that small molecules that block HER2/HER3 KD association would be most likely to block the oncogenic effects of concurrent HER2^{missense}/HER3^{E928G} mutations. To the best of our knowledge, clinical compounds that disrupt HER2/HER3 KD heterodimerization have not been reported. In the absence of such a molecule, we hypothesized that the combination of a HER2 TKI + PI3K α inhibitor would block the increased oncogenicity caused by co-occurring *HER2* and *HER3* mutations. Indeed, the combination of neratinib and alpelisib strongly reduced growth and invasion of double-mutant cells. Similarly, the combination of HER2 and PI3K α inhibitors has been suggested for *HER2*-amplified breast cancers harboring *PIK3CA* mutations (Hanker et al., 2013; Rexer et al., 2014). While initial clinical trials indicated that the combination of a pan-PI3K inhibitor with the HER2 TKI lapatinib resulted in significant toxicities (Guerin et al., 2017), a recent trial suggested that the combination of the HER2 antibody-drug conjugate T-DM1 and a more specific PI3K α inhibitor is tolerable (Jain et al., 2018). Our results suggest that single-agent HER2 TKIs may not sufficiently block the growth of *HER2*-mutant tumors with co-occurring *HER3* mutations. Therefore, clinical trials investigating the efficacy and safety of combining an HER2 TKI and PI3K α inhibitor are warranted in cancers harboring co-occurring *HER2/HER3* mutations.

STAR★METHODS

Detailed methods are provided in the online version of this paper and include the following:

- KEY RESOURCES TABLE
- RESOURCE AVAILABILITY
 - Lead contact
 - Materials availability
 - Data and code availability
- EXPERIMENTAL MODELS AND SUBJECT DETAILS
 - Cell lines
 - Mouse models
- METHOD DETAILS
 - Database searches
 - Computational modeling
 - Structural modeling of the HER2-HER3 heterodimer
 - Molecular docking of HER2 protein and ligand (neratinib)
 - Classical MD simulations
 - Conformational free energy calculations
 - Protein-ligand free energy calculations
 - Protein-protein interface energy

- Plasmids
- Transient transfections
- Lentiviral infections
- Immunoprecipitation
- Proximity ligation assay
- Western blot analysis
- Flow cytometry
- Organoid establishment and culture
- Sanger sequencing of *ERBB2* and *ERBB3*
- Quantitative RT-PCR
- Cell viability assay and IC₅₀ estimation
- Cell proliferation assay
- Three-dimensional morphogenesis assay
- Cell invasion assay
- Xenograft Studies
- **QUANTIFICATION AND STATISTICAL ANALYSIS**

SUPPLEMENTAL INFORMATION

Supplemental information can be found online at <https://doi.org/10.1016/j.ccell.2021.06.001>.

ACKNOWLEDGMENTS

We thank Ben Park for providing the MCF7 HER2^{WT}, HER2^{L755S}, and HER2^{V777L} isogenic cell lines, Samuel Aparicio for providing the SA493 breast cancer PDX, the UTSW Moody Foundation Flow Cytometry Facility, and members of the Arteaga and Meiler Laboratories and Christine Lovly for helpful discussions. This study was supported by NCI grant R01CA224899 (to A.B.H. and C.L.A.), the NCI/UTSW Simmons Cancer Center P30 CA142543, CPRIT RR170061 grant (to C.L.A.), NCI Breast SPOR grant P50 CA098131, the NCI/Vanderbilt-Ingram Cancer Center P30 CA68485, the Susan G. Komen Breast Cancer Foundation grant SAB1800010 (to C.L.A.), and grants from the Breast Cancer Research Foundation (to A.B.H. and C.L.A.). B.P.B. is supported through the NIH by a Ruth L. Kirschstein NRSA fellowship (F30DK118774).

AUTHOR CONTRIBUTIONS

Conceptualization, A.B.H., J.M., and C.L.A.; methodology, A.B.H., B.P.B., H.S.J., A.M., D.Y., C.-C.L., K.-M.L., S.C., D.R.S., A.S., J.P.K., and J.H.S.; formal analysis, B.P.B.; investigation, A.B.H., B.P.B., A.M., D.Y., C.-C.L., H.A., K.-M.L., S.C., A.S., and J.P.K.; resources, D.Y., C.-C.L., S.C., D.R.S., M.R.B., J.H., and A.S.L.; data curation, A.B.H., B.P.B., and J.H.; writing – original draft, A.B.H., B.P.B., and H.S.J.; writing – review & editing, A.B.H., B.P.B., J.M., H.S.J., D.R.S., A.S., M.R.B., and C.L.A.; supervision, A.B.H., J.M., and C.L.A.; project management, A.B.H., J.M., and C.L.A.; funding acquisition, A.B.H., J.M., and C.L.A.

DECLARATION OF INTERESTS

A.B.H. receives or has received research grant support from Takeda and Lilly and travel support from Puma Biotechnology. J.H. is an employee of Foundation Medicine. A.S.L. is an employee of and holds ownership interest (including patents) in Puma Biotechnology, Inc. C.L.A. receives or has received research grant support from Pfizer, Lilly, Radius, Bayer, and Takeda, holds stock options in Provista, and serves or has served in a scientific advisory role to Puma Biotechnology, Novartis, Lilly, TAIHO Oncology, Daiichi Sankyo, Merck, AstraZeneca, OrigimMed, Immunomedics, Athenex, Arvinas, and the Susan G. Komen Foundation. All other authors declare no competing interests.

Received: September 9, 2020

Revised: February 28, 2021

Accepted: June 2, 2021

Published: June 24, 2021

REFERENCES

- Aertgeerts, K., Skene, R., Yano, J., Sang, B.C., Zou, H., Snell, G., Jennings, A., Iwamoto, K., Habuka, N., Hirokawa, A., et al. (2011). Structural analysis of the mechanism of inhibition and allosteric activation of the kinase domain of HER2 protein. *J. Biol. Chem.* 286, 18756–18765.
- Agus, D.B., Akita, R.W., Fox, W.D., Lewis, G.D., Higgins, B., Pisacane, P.I., Lofgren, J.A., Tindell, C., Evans, D.P., Maiese, K., et al. (2002). Targeting ligand-activated ErbB2 signaling inhibits breast and prostate tumor growth. *Cancer Cell* 2, 127–137.
- Arteaga, C.L., and Engelman, J.A. (2014). ERBB receptors: from oncogene discovery to basic science to mechanism-based cancer therapeutics. *Cancer Cell* 25, 282–303.
- Bender, B.J., Cisneros, A., Duran, A.M., Finn, J.A., Fu, D., Lokits, A.D., Mueller, B.K., Sangha, A.K., Sauer, M.F., Sevy, A.M., et al. (2016). Protocols for molecular modeling with Rosetta3 and RosettaScripts. *Biochemistry* 55, 4748–4763.
- Bose, R., Kavuri, S.M., Searleman, A.C., Shen, W., Shen, D., Koboldt, D.C., Monsey, J., Goel, N., Aronson, A.B., Li, S., et al. (2013). Activating HER2 mutations in HER2 gene amplification negative breast cancer. *Cancer Discov.* 3, 224–237.
- Cancer Genome Atlas, N. (2012). Comprehensive molecular portraits of human breast tumours. *Nature* 490, 61–70.
- Case, D.A., Ben-Shalom, I.Y., Brozell, S.R., Cerutti, D.S., Cheatham, T.E., III, Cruzeiro, V.W.D., Darden, T.A., Duke, R.E., Ghoreishi, D., Gilson, M.K., et al. (2018). AMBER 2018 (University of California).
- Cerami, E., Gao, J., Dogrusoz, U., Gross, B.E., Sumer, S.O., Aksoy, B.A., Jacobsen, A., Byrne, C.J., Heuer, M.L., Larsson, E., et al. (2012). The cBio cancer genomics portal: an open platform for exploring multidimensional cancer genomics data. *Cancer Discov.* 2, 401–404.
- Chakrabarty, A., Rexer, B.N., Wang, S.E., Cook, R.S., Engelman, J.A., and Arteaga, C.L. (2010). H1047R phosphatidylinositol 3-kinase mutant enhances HER2-mediated transformation by heregulin production and activation of HER3. *Oncogene* 29, 5193–5203.
- Chakrabarty, A., Sanchez, V., Kuba, M.G., Rinehart, C., and Arteaga, C.L. (2012). Feedback upregulation of HER3 (ErbB3) expression and activity attenuates antitumor effect of PI3K inhibitors. *Proc. Natl. Acad. Sci. U S A* 109, 2718–2723.
- Chandralapathy, S., Sawai, A., Scaltriti, M., Rodrik-Outmezguine, V., Grbovic-Huezo, O., Serra, V., Majumder, P.K., Baselga, J., and Rosen, N. (2011). AKT inhibition relieves feedback suppression of receptor tyrosine kinase expression and activity. *Cancer Cell* 19, 58–71.
- Choi, B., Cha, M., Eun, G.S., Lee, D.H., Lee, S., Ehsan, M., Chae, P.S., Heo, W.D., Park, Y., and Yoon, T.Y. (2020). Single-molecule functional anatomy of endogenous HER2-HER3 heterodimers. *eLife* 9, e53934.
- Chou, T.-C. (2010). Drug combination studies and their synergy quantification using the Chou-Talalay method. *Cancer Res.* 70, 440.
- Cocco, E., Javier Carmona, F., Razavi, P., Won, H.H., Cai, Y., Rossi, V., Chan, C., Cownie, J., Soong, J., Toska, E., et al. (2018). Neratinib is effective in breast tumors bearing both amplification and mutation of ERBB2 (HER2). *Sci. Signal.* 11, eaat9773.
- Cocco, E., Lopez, S., Santin, A.D., and Scaltriti, M. (2019). Prevalence and role of HER2 mutations in cancer. *Pharmacol. Ther.* 199, 188–196.
- Collier, T.S., Diraviyam, K., Monsey, J., Shen, W., Sept, D., and Bose, R. (2013). Carboxyl group footprinting mass spectrometry and molecular dynamics identify key interactions in the HER2-HER3 receptor tyrosine kinase interface. *J. Biol. Chem.* 288, 25254–25264.
- Combs, S.A., DeLuca, S.L., DeLuca, S.H., Lemmon, G.H., Nannemann, D.P., Nguyen, E.D., Willis, J.R., Sheehan, J.H., and Meiler, J. (2013). Small-molecule ligand docking into comparative models with Rosetta. *Nat. Protoc.* 8, 1277–1298.
- Consortium, A.P.G. (2017). AACR Project GENIE: powering precision medicine through an international consortium. *Cancer Discov.* 7, 818–831.

- Cornell, W.D., Cieplak, P., Bayly, C.I., and Kollman, P.A. (1993). Application of RESP charges to calculate conformational energies, hydrogen bond energies, and free energies of solvation. *J. Am. Chem. Soc.* **115**, 9620–9631.
- Croessmann, S., Formisano, L., Kinch, L.N., Gonzalez-Ericsson, P.I., Sudhan, D.R., Nagy, R.J., Mathew, A., Bernicker, E.H., Cristofanilli, M., He, J., et al. (2019). Combined blockade of activating ERBB2 mutations and ER results in synthetic lethality of ER+/HER2 mutant breast cancer. *Clin. Cancer Res.* **25**, 277–289.
- Debnath, J., Muthuswamy, S.K., and Brugge, J.S. (2003). Morphogenesis and oncogenesis of MCF-10A mammary epithelial acini grown in three-dimensional basement membrane cultures. *Methods* **30**, 256–268.
- DeLuca, S., Khar, K., and Meiler, J. (2015). Fully flexible docking of medium sized ligand libraries with RosettaLigand. *PLoS One* **10**, e0132508.
- Deniziaut, G., Tille, J.C., Bidard, F.C., Vacher, S., Schnitzler, A., Chemlali, W., Tremoulet, L., Fuhrmann, L., Cottu, P., Rouzier, R., et al. (2016). ERBB2 mutations associated with solid variant of high-grade invasive lobular breast carcinomas. *Oncotarget* **7**, 73337–73346.
- Desmedt, C., Zoppoli, G., Gundem, G., Pruneri, G., Larsimont, D., Fornili, M., Fumagalli, D., Brown, D., Rothe, F., Vincent, D., et al. (2016). Genomic characterization of primary invasive lobular breast cancer. *J. Clin. Oncol.* **34**, 1872–1881.
- Eirew, P., Steif, A., Khattra, J., Ha, G., Yap, D., Farahani, H., Gelmon, K., Chia, S., Mar, C., Wan, A., et al. (2015). Dynamics of genomic clones in breast cancer patient xenografts at single-cell resolution. *Nature* **518**, 422–426.
- Frenz, B., Lewis, S.M., King, I., DiMaio, F., Park, H., and Song, Y. (2020). Prediction of protein mutational free energy: benchmark and sampling improvements increase classification accuracy. *Front. Bioeng. Biotechnol.* **8**, 558247.
- Gorelick, A.N., Sánchez-Rivera, F.J., Cai, Y., Bielski, C.M., Biederstedt, E., Jonsson, P., Richards, A.L., Vasan, N., Penson, A.V., Friedman, N.D., et al. (2020). Phase and context shape the function of composite oncogenic mutations. *Nature* **582**, 100–103.
- Greulich, H., Kaplan, B., Mertins, P., Chen, T.H., Tanaka, K.E., Yun, C.H., Zhang, X., Lee, S.H., Cho, J., Ambrogio, L., et al. (2012). Functional analysis of receptor tyrosine kinase mutations in lung cancer identifies oncogenic extracellular domain mutations of ERBB2. *Proc. Natl. Acad. Sci. U S A* **109**, 14476–14481.
- Grossfield, A. WHAM: the weighted histogram analysis method, version 2.0.10, http://membrane.urmc.rochester.edu/wordpress/?page_id=126.
- Guerin, M., Rezai, K., Isambert, N., Campone, M., Autret, A., Pakradouni, J., Provansal, M., Camerlo, J., Sabatier, R., Bertucci, F., et al. (2017). PIKHER2: a phase IB study evaluating buparlisib in combination with lapatinib in trastuzumab-resistant HER2-positive advanced breast cancer. *Eur. J. Cancer* **86**, 28–36.
- Haikala, H.M., and Janne, P.A. (2021). 30 years of HER3: from basic biology to therapeutic interventions. *Clin. Cancer Res.* **4465**, 2020.
- Hanker, A.B., Brewer, M.R., Sheehan, J.H., Koch, J.P., Sliwoski, G.R., Nagy, R., Lanman, R., Berger, M.F., Hyman, D.M., Solit, D.B., et al. (2017). An acquired HER2(t798I) gatekeeper mutation induces resistance to neratinib in a patient with HER2 mutant-driven breast cancer. *Cancer Discov.* **7**, 575–585.
- Hanker, A.B., Pfefferle, A.D., Balko, J.M., Kuba, M.G., Young, C.D., Sanchez, V., Sutton, C.R., Cheng, H., Perou, C.M., Zhao, J.J., et al. (2013). Mutant PIK3CA accelerates HER2-driven transgenic mammary tumors and induces resistance to combinations of anti-HER2 therapies. *Proc. Natl. Acad. Sci. U S A* **110**, 14372–14377.
- Holbro, T., Beerli, R.R., Maurer, F., Koziczak, M., Barbas, C.F., 3rd, and Hynes, N.E. (2003). The ErbB2/ErbB3 heterodimer functions as an oncogenic unit: ErbB2 requires ErbB3 to drive breast tumor cell proliferation. *Proc. Natl. Acad. Sci. U S A* **100**, 8933–8938.
- Hyman, D.M., Piha-Paul, S.A., Won, H., Rodon, J., Saura, C., Shapiro, G.I., Juric, D., Quinn, D.I., Moreno, V., Doger, B., et al. (2018). HER kinase inhibition in patients with HER2- and HER3-mutant cancers. *Nature* **554**, 189–194.
- Jacobsen, H.J., Poulsen, T.T., Dahlman, A., Kjaer, I., Koefoed, K., Sen, J.W., Weiguny, D., Bjerregaard, B., Andersen, C.R., Horak, I.D., et al. (2015). Pan-HER, an antibody mixture simultaneously targeting EGFR, HER2, and HER3, effectively overcomes tumor heterogeneity and plasticity. *Clin. Cancer Res.* **21**, 4110–4122.
- Jain, S., Shah, A.N., Santa-Maria, C.A., Siziopikou, K., Rademaker, A., Helenowski, I., Cristofanilli, M., and Gradishar, W.J. (2018). Phase I study of alpelisib (BYL-719) and trastuzumab emtansine (T-DM1) in HER2-positive metastatic breast cancer (MBC) after trastuzumab and taxane therapy. *Breast Cancer Res. Treat.* **171**, 371–381.
- Jaiswal, B.S., Kljavin, N.M., Stawiski, E.W., Chan, E., Parikh, C., Durinck, S., Chaudhuri, S., Pujara, K., Guillory, J., Edgar, K.A., et al. (2013). Oncogenic ERBB3 mutations in human cancers. *Cancer Cell* **23**, 603–617.
- Junttila, T.T., Akita, R.W., Parsons, K., Fields, C., Lewis Phillips, G.D., Friedman, L.S., Sampath, D., and Sliwkowski, M.X. (2009). Ligand-independent HER2/HER3/PI3K complex is disrupted by trastuzumab and is effectively inhibited by the PI3K inhibitor GDC-0941. *Cancer Cell* **15**, 429–440.
- Kavuri, S.M., Jain, N., Galimi, F., Cottino, F., Leto, S.M., Migliardi, G., Searleman, A.C., Shen, W., Monsey, J., Trusolino, L., et al. (2015). HER2 activating mutations are targets for colorectal cancer treatment. *Cancer Discov.* **5**, 832–841.
- Kloth, M., Ruesseler, V., Engel, C., Koenig, K., Peifer, M., Mariotti, E., Kuenstlinger, H., Florin, A., Rommelscheidt-Fuss, U., Koitzsch, U., et al. (2016). Activating ERBB2/HER2 mutations indicate susceptibility to pan-HER inhibitors in Lynch and Lynch-like colorectal cancer. *Gut* **65**, 1296–1305.
- Koehler Leman, J., and Bonneau, R. (2018). A novel domain assembly routine for creating full-length models of membrane proteins from known domain structures. *Biochemistry* **57**, 1939–1944.
- Kurozumi, S., Alsalem, M., Monteiro, C.J., Bhardwaj, K., Joosten, S.E.P., Fujii, T., Shirabe, K., Green, A.R., Ellis, I.O., Rakha, E.A., et al. (2020). Targetable ERBB2 mutation status is an independent marker of adverse prognosis in estrogen receptor positive, ERBB2 non-amplified primary lobular breast carcinoma: a retrospective in silico analysis of public datasets. *Breast Cancer Res.* **22**, 85.
- Leman, J.K., Weitzner, B.D., Lewis, S.M., Adolf-Bryfogle, J., Alam, N., Alford, R.F., Aprahamian, M., Baker, D., Barlow, K.A., Barth, P., et al. (2020). Macromolecular modeling and design in Rosetta: recent methods and frameworks. *Nat. Methods* **17**, 665–680.
- Li, J., Xiao, Q., Bao, Y., Wang, W., Goh, J., Wang, P., and Yu, Q. (2019). HER2-L755S mutation induces hyperactive MAPK and PI3K-mTOR signaling, leading to resistance to HER2 tyrosine kinase inhibitor treatment. *Cell Cycle* **18**, 1513–1522.
- Littlefield, P., Liu, L., Mysore, V., Shan, Y., Shaw, D.E., and Jura, N. (2014). Structural analysis of the EGFR/HER3 heterodimer reveals the molecular basis for activating HER3 mutations. *Sci. Signal.* **7**, ra114.
- Ma, C.X., Bose, R., Gao, F., Freedman, R.A., Telli, M.L., Kimmick, G., Winer, E., Naughton, M., Goetz, M.P., Russell, C., et al. (2017). Neratinib efficacy and circulating tumor DNA detection of HER2 mutations in HER2 nonamplified metastatic breast cancer. *Clin. Cancer Res.* **23**, 5687–5695.
- Maier, J.A., Martinez, C., Kasavajhala, K., Wickstrom, L., Hauser, K.E., and Simmerling, C. (2015). ff14SB: improving the accuracy of protein side chain and backbone parameters from ff99SB. *J. Chem. Theor. Comput.* **11**, 3696–3713.
- Meiler, J., and Baker, D. (2005). The fumarate sensor DcuS: progress in rapid protein fold elucidation by combining protein structure prediction methods with NMR spectroscopy. *J. Magn. Reson.* **173**, 310–316.
- Mendenhall, J., Brown, B.P., Kothiwale, S., and Meiler, J. (2020). BCL::Conf: improved open-source knowledge-based conformation sampling using the crystallography open database. *J. Chem. Inf. Model.* **61**, 189–201.
- Miller, B.R., McGee, T.D., Swails, J.M., Homeyer, N., Gohlke, H., and Roitberg, A.E. (2012). MMPBSA.py: an efficient program for end-state free energy calculations. *J. Chem. Theor. Comput.* **8**, 3314–3321.
- Mishra, R., Hanker, A.B., and Garrett, J.T. (2017). Genomic alterations of ERBB receptors in cancer: clinical implications. *Oncotarget* **8**, 114371–114392.

- Nagano, M., Kohsaka, S., Ueno, T., Kojima, S., Saka, K., Iwase, H., Kawazu, M., and Mano, H. (2018). High-throughput functional evaluation of variants of unknown significance in ERBB2. *Clin. Cancer Res.* 24, 5112–5122.
- Nayar, U., Cohen, O., Kapstad, C., Cuoco, M.S., Waks, A.G., Wander, S.A., Painter, C., Freeman, S., Persky, N.S., Marini, L., et al. (2019). Acquired HER2 mutations in ER(+) metastatic breast cancer confer resistance to estrogen receptor-directed therapies. *Nat. Genet.* 51, 207–216.
- Ping, Z., Siegal, G.P., Harada, S., Eltoum, I.E., Youssef, M., Shen, T., He, J., Huang, Y., Chen, D., Li, Y., et al. (2016). ERBB2 mutation is associated with a worse prognosis in patients with CDH1 altered invasive lobular cancer of the breast. *Oncotarget* 7, 80655–80663.
- Prado Martins, R., Findakly, S., Daskalogianni, C., Teulade-Fichou, M.-P., Blondel, M., and Fähræus, R. (2018). In cellulo protein-mRNA interaction assay to determine the action of G-quadruplex-binding molecules. *Molecules* 23, 3124.
- Razavi, P., Chang, M.T., Xu, G., Bandlamudi, C., Ross, D.S., Vasan, N., Cai, Y., Bielski, C.M., Donoghue, M.T.A., Jonsson, P., et al. (2018). The genomic landscape of endocrine-resistant advanced breast cancers. *Cancer Cell* 34, 427–438 e426.
- Red Brewer, M., Yun, C.H., Lai, D., Lemmon, M.A., Eck, M.J., and Pao, W. (2013). Mechanism for activation of mutated epidermal growth factor receptors in lung cancer. *Proc. Natl. Acad. Sci. U S A* 110, E3595–E3604.
- Rexer, B.N., Chanthaphaychith, S., Dahlman, K., and Arteaga, C.L. (2014). Direct inhibition of PI3K in combination with dual HER2 inhibitors is required for optimal antitumor activity in HER2+ breast cancer cells. *Breast Cancer Res.* 16, R9.
- Robichaux, J.P., Elamin, Y.Y., Vijayan, R.S.K., Nilsson, M.B., Hu, L., He, J., Zhang, F., Pisegna, M., Poteete, A., Sun, H., et al. (2019). Pan-cancer landscape and analysis of ERBB2 mutations identifies poziotinib as a clinically active inhibitor and enhancer of T-DM1 activity. *Cancer Cell* 36, 444–457 e447.
- Roe, D.R., and Cheatham, T.E. (2013). PTRAJ and CPPTRAJ: software for processing and analysis of molecular dynamics trajectory data. *J. Chem. Theor. Comput.* 9, 3084–3095.
- Ross, J.S., Wang, K., Sheehan, C.E., Boguniewicz, A.B., Otto, G., Downing, S.R., Sun, J., He, J., Curran, J.A., Ali, S., et al. (2013). Relapsed classic E-cadherin (CDH1)-mutated invasive lobular breast cancer shows a high frequency of HER2 (ERBB2) gene mutations. *Clin. Cancer Res.* 19, 2668–2676.
- Saito, Y., Koya, J., Araki, M., Kogure, Y., Shingaki, S., Tabata, M., McClure, M.B., Yoshifuji, K., Matsumoto, S., Isaka, Y., et al. (2020). Landscape and function of multiple mutations within individual oncogenes. *Nature* 582, 95–99.
- Samuels, Y., Diaz, L.A., Jr., Schmidt-Kittler, O., Cummins, J.M., Delong, L., Cheong, I., Rago, C., Huso, D.L., Lengauer, C., Kinzler, K.W., et al. (2005). Mutant PIK3CA promotes cell growth and invasion of human cancer cells. *Cancer Cell* 7, 561–573.
- Smirnova, T., Zhou, Z.N., Flinn, R.J., Wyckoff, J., Boimel, P.J., Pozzuto, M., Coniglio, S.J., Backer, J.M., Bresnick, A.R., Condeelis, J.S., et al. (2012). Phosphoinositide 3-kinase signaling is critical for ErbB3-driven breast cancer cell motility and metastasis. *Oncogene* 31, 706–715.
- Smith, S.T., and Meiler, J. (2020). Assessing multiple score functions in Rosetta for drug discovery. *PLoS One* 15, e0240450.
- Smyth, L.M., Piha-Paul, S.A., Won, H.H., Schram, A.M., Saura, C., Loi, S., Lu, J., Shapiro, G.I., Juric, D., Mayer, I.A., et al. (2020). Efficacy and determinants of response to HER kinase inhibition in HER2-mutant metastatic breast cancer. *Cancer Discov.* 10, 198–213.
- Sogabe, S., Kawakita, Y., Igaki, S., Iwata, H., Miki, H., Cary, D.R., Takagi, T., Takagi, S., Ohta, Y., and Ishikawa, T. (2012). Structure-based approach for the discovery of pyrrolo[3,2-d]pyrimidine-based EGFR T790M/L858R mutant inhibitors. *ACS Med. Chem. Lett.* 4, 201–205.
- Song, Y., DiMaio, F., Wang, R.Y.-R., Kim, D., Miles, C., Brunette, T.J., Thompson, J., and Baker, D. (2013). High-resolution comparative modeling with RosettaCM. *Structure* 21, 1735–1742.
- Sudhan, D.R., Guerrero-Zotano, A., Won, H., González Ericsson, P., Servetto, A., Huerta-Rosario, M., Ye, D., Lee, K.M., Formisano, L., Guo, Y., et al. (2020). Hyperactivation of TORC1 drives resistance to the pan-HER tyrosine kinase inhibitor neratinib in HER2-mutant cancers. *Cancer Cell* 37, 183–199.e185.
- Vasan, N., Razavi, P., Johnson, J.L., Shao, H., Shah, H., Antoine, A., Ladewig, E., Gorelick, A., Lin, T.Y., Toska, E., et al. (2019). Double PIK3CA mutations in *cis* increase oncogenicity and sensitivity to PI3K α inhibitors. *Science* 366, 714–723.
- Vega, C., and Abascal, J.L.F. (2011). Simulating water with rigid non-polarizable models: a general perspective. *PCCP* 13, 19663–19688.
- Wallasch, C., Weiss, F.U., Niederfellner, G., Jallat, B., Issing, W., and Ullrich, A. (1995). Heregulin-dependent regulation of HER2/neu oncogenic signaling by heterodimerization with HER3. *EMBO J.* 14, 4267–4275.
- Wang, T., Xu, Y., Sheng, S., Yuan, H., Ouyang, T., Li, J., Wang, T., Fan, Z., Fan, T., Lin, B., and Xie, Y. (2017). HER2 somatic mutations are associated with poor survival in HER2-negative breast cancers. *Cancer Sci.* 108, 671–677.
- Weiser, J., Shenkin, P.S., and Still, W.C. (1999). Approximate atomic surfaces from linear combinations of pairwise overlaps (LCPO). *J. Comput. Chem.* 20, 217–230.
- Xu, X., De Angelis, C., Burke, K.A., Nardone, A., Hu, H., Qin, L., Veeraraghavan, J., Sethunath, V., Heiser, L.M., Wang, N., et al. (2017). HER2 reactivation through acquisition of the HER2 L755S mutation as a mechanism of acquired resistance to HER2-targeted therapy in HER2(+) breast cancer. *Clin. Cancer Res.* 23, 5123–5134.
- Xue, C., Liang, F., Mahmood, R., Vuolo, M., Wyckoff, J., Qian, H., Tsai, K.L., Kim, M., Locker, J., Zhang, Z.Y., and Segall, J.E. (2006). ErbB3-dependent motility and intravasation in breast cancer metastasis. *Cancer Res.* 66, 1418–1426.
- Yarden, Y., and Sliwkowski, M.X. (2001). Untangling the ErbB signalling network. *Nat. Rev. Mol. Cell Biol.* 2, 127–137.
- Zabransky, D.J., Yankaskas, C.L., Cochran, R.L., Wong, H.Y., Croessmann, S., Chu, D., Kavuri, S.M., Red Brewer, M., Rosen, D.M., Dalton, W.B., et al. (2015). HER2 missense mutations have distinct effects on oncogenic signaling and migration. *Proc. Natl. Acad. Sci. U S A* 112, E6205–E6214.
- Zhang, X., Gureasko, J., Shen, K., Cole, P.A., and Kuriyan, J. (2006). An allosteric mechanism for activation of the kinase domain of epidermal growth factor receptor. *Cell* 125, 1137–1149.

STAR★METHODS

KEY RESOURCES TABLE

REAGENT or RESOURCE	SOURCE	IDENTIFIER
Antibodies		
pHER2 (Y1221/2)	Cell Signaling Technologies	Cat# 2243; RRID: AB_490899
HER2 (western blot)	Cell Signaling Technologies	Cat# 2242; RRID: AB_331015
HER2 (IP)	Thermo Fisher Scientific	Cat# MS-730-P1-A; RRID: AB_141773
pHER3 (Y1289)	Cell Signaling Technologies	Cat# 4791; RRID: AB_2099709
pHER3 (Y1197)	Cell Signaling Technologies	Cat# 4561; RRID: AB_2099707
HER3	Cell Signaling Technologies	Cat# 12708; RRID: AB_2721919
pAkt (S473)	Cell Signaling Technologies	Cat# 9271; RRID: AB_329825
pAkt (T308)	Cell Signaling Technologies	Cat# 13038; RRID: AB_2629447
pERK1/2 T202/Y204	Cell Signaling Technologies	Cat# 9101; RRID: AB_331646
pS6 (240/4)	Cell Signaling Technologies	Cat# 2215; RRID: AB_331682
pS6 (235/6)	Cell Signaling Technologies	Cat# 2211; RRID: AB_331679
β-actin	Cell Signaling Technologies	Cat# 4970; RRID: AB_2223172
Trastuzumab	UT Southwestern Pharmacy	N/A
Pertuzumab	Vanderbilt University Medical Center Pharmacy	N/A
Sym013 (PanHER)	Symphogen	N/A
CD298 (biotin-conjugated)	Miltenyi Biotec	Cat# 130-101-292; RRID: AB_2657045
Goat anti-Human IgG (H+L) Cross-Adsorbed Secondary Antibody, Alexa Fluor 647	Thermo Fisher Scientific	Cat# A-21445; RRID: AB_2535862
Bacterial and Virus Strains		
One Shot™ MAX Efficiency™ DH5α™-T1	Thermo Fisher Scientific	Cat# 12297016
One Shot™ Stbl3™ Chemically Competent cells	Thermo Fisher Scientific	Cat# C737303
Biological Samples		
SA493 (<i>HER2S310F</i>) breast cancer PDX	Gift from Samuel Aparicio, University of British Columbia	N/A
Recombinant DNA		
pDONR223_HER2_WT	Addgene	#81892; RRID: Addgene_81892
pDONR223_HER3_WT	Addgene	#82114; RRID: Addgene_82114
HER2_WT_ICD	PMID: 24019492	N/A
HER3_WT_ICD	PMID: 28274957	N/A
pLX302 vector	Addgene	#25896; RRID: Addgene_25896
pLX304 vector	Addgene	#25890; RRID: Addgene_25890
psPAX2	Addgene	#12260; RRID: Addgene_12260
pMD2.G	Addgene	#12259; RRID: Addgene_12259
Chemicals, Peptides, and Recombinant Proteins		
Puromycin Dihydrochloride	Thermo Fisher Scientific	Cat# A1113803
Blasticidin S HCl	Thermo Fisher Scientific	Cat# A1113903
Recombinant Human Heregulin Beta-1	PeptoTech	Cat# 100-03
Growth Factor-reduced Matrigel	Thermo Fisher Scientific	Cat# 354230
Neratinib (HKI-272)	PUMA biotechnology / Selleck Chemicals	Cat# S2150
Alpelisib (BYL719)	Selleck Chemicals	Cat# S2814
Buparlisib (BKM120)	Selleck Chemicals	Cat# S2247

(Continued on next page)

Continued

REAGENT or RESOURCE	SOURCE	IDENTIFIER
Afatinib (BIBW2992)	Selleck Chemicals	Cat# S7810
Poziotinib	Selleck Chemicals	Cat# S7358
Tucatinib (ONT-380)	Selleck Chemicals	Cat# S8362
Lipofectamine™ 2000 Transfection Reagent	Thermo Fisher Scientific	Cat# 11668019
Lipofectamine™ RNAiMAX Transfection Reagent	Thermo Fisher Scientific	Cat# 13778150

Critical Commercial Assays

Gateway LR Clonase II Enzyme Mix	Thermo Fisher Scientific	Cat# 11-791-020
Maxwell® RSC simplyRNA Cells Kit	Promega	Cat# AS1390
Iscrip™ cDNA Synthesis Kit	Bio-Rad	Cat# 1708891
Applied Biosystems PowerUp SYBR Green Master Mix	Thermo Fisher Scientific	Cat# A25741
CellTiterGlo® Luminescent Cell Viability Assay	Promega	Cat# G7571
CyQUANT™ Cell Proliferation Assay Kit	Thermo Fisher Scientific	Cat# C7026
Corning® BioCoat™ Matrigel® Invasion Chambers, Corning®, Growth Factor Reduced Corning Matrigel™	Corning	Cat# 354483
Dynabeads™ Protein G Immunoprecipitation Kit	Thermo Fisher Scientific	Cat# 10007D
Maxwell® RSC simplyRNA Cells Kit	Promega	Cat# AS1390
RNeasy Micro Kit	Qiagen	Cat# 74004
Duolink® In Situ Red Starter Kit Mouse/Rabbit	Sigma-Aldrich	Cat #DUO92101
CellTiter-Glo® 3D Cell Viability Assay	Promega	Cat# G9683
EasySep human biotin positive selection kit II	STEMCELL Technologies	Cat# 17663

Deposited Data

NA

Experimental Models: Cell Lines

Invitrogen 293FT Cell Line	Thermo Fisher Scientific	Cat# R70007
HEK-293 cell line	ATCC	Cat# CRL-1573; RRID: CVCL_0045
MCF 10A cell line	ATCC	Cat# CRL-10317; RRID: CVCL_0598
MCF7 isogenic <i>HER2</i> ^{WT} , <i>HER2</i> ^{L755S} , <i>HER2</i> ^{V777L} cell lines	Gifts from Dr. Ben Ho Park, Vanderbilt-Ingram Cancer Center	N/A
OVCAR8 <i>HER2</i> ^{G776V} cell line	DCDT Tumor Repository, NCI	N/A
CW-2 <i>HER2</i> ^{L755S} / <i>HER3</i> ^{E928G} cell line	RIKEN	Cat# RCB0778; RRID: CVCL_1151

Oligonucleotides

siHER2_2264T>C_1: 5' AAAGUGUCGAGGGAAAACatt	Thermo Fisher Scientific	N/A
siHER2_2264T>C_2: 5' AAGUGUCGAGGGAAAACact	Thermo Fisher Scientific	N/A
siHER3_1	Cell Signaling Technologies	Cat# 6504
siHER3_2	Cell Signaling Technologies	Cat# 6422
AllStars Negative Control siRNA	Qiagen	Cat# 1027280
ERBB2_2264T>C_F: 5'CAGTGGCCATCAACGTGTC (qPCR)	IDT	N/A
ERBB2_2264T>C_R: 5'TACACCAGTTCAGCAGGTCCT	IDT	N/A
ERBB2 (WT; qPCR)	Qiagen	Cat# PPH00209B
ERBB3 (WT;qPCR)	Qiagen	Cat# PPH00463B

Software and Algorithms

GraphPad Prism 8.3 software	GraphPad, San Diego	RRID: SCR_002798
Gelcount software	Oxford Optronix	N/A
FlowJo software	BD Bioscience	RRID: SCR_008520
Image Lab software	Bio_rad	N/A
Image J software	NIH	RRID: SCR_003070
CompuSyn software	PMID:20068163	N/A
Rosetta 3.12	Rosetta Commons	RRID: SCR_015701

(Continued on next page)

Continued

REAGENT or RESOURCE	SOURCE	IDENTIFIER
AMBER18	University of California, San Francisco	N/A
Gaussian09 D.01	Carnegie Mellon University; Gaussian, Inc	N/A
PyMOL 2.2	Schrodinger Inc DeLano Scientific LLC	RRID: SCR_000305
LFEP	Moradi Lab, University of Arkansas	N/A

RESOURCE AVAILABILITY

Lead contact

Further information and requests for resources and reagents should be directed to and will be fulfilled by the Lead Contact, Dr. Ariella Hanker (ariella.hanker@utsouthwestern.edu).

Materials availability

Plasmids generated in this study will be deposited to Addgene upon request. There are restrictions to the availability of the SA493-derived organoids due to the terms of our MTA with British Columbia Cancer Agency. There are restrictions to the availability of the *HER2*-mutant isogenic MCF7 cell lines stably expressing *HER3* due to the terms of our MTA with Dr. Ben Ho Park.

Data and code availability

The cBioPortal and Project GENIE datasets are available at www.cBioPortal.org and www.cBioPortal.org/GENIE, respectively. The published article includes the dataset analyzed from Foundation Medicine. Table S1 includes the list of co-occurring *HER2/HER3* mutations found in breast cancers. Structural 3D coordinate data from PDB and PubChem were downloaded from <https://www.rcsb.org/> and <https://pubchem.ncbi.nlm.nih.gov/>, respectively. Our predicted all-atom computational structural models of the *HER2/HER3* near-full-length heterodimer are available for free at https://github.com/meilerlab/computational_models.

EXPERIMENTAL MODELS AND SUBJECT DETAILS

Cell lines

MCF10A and HEK293 cells were purchased from ATCC. Cell lines were authenticated by ATCC prior to purchase by the short tandem repeat method. 293FT cells were purchased from Invitrogen. MCF-7 cells were previously isogenically modified using AAV-mediated gene targeting to include *HER2*^{L755S}, *HER2*^{V777L}, or targeted *HER2*^{WT} (Zabransky et al., 2015). OVCAR8 cells were purchased from DCDT tumor repository, NCI. CW2 cells were purchased from Riken Bioresource Research Center. *ERBB2*^{L755S} and *ERBB3*^{E928G} heterozygous mutations were confirmed by Sanger sequencing of cDNA derived from CW2 cells.

MCF7, 293FT, and HEK293 cells were maintained in DMEM supplemented with 10% FBS and 1x antibiotic-antimycotic. OVCAR8 and CW2 cells were maintained in RPMI1640 supplemented with 10% FBS and 1x antibiotic-antimycotic. MCF10A cells were maintained in MCF10A complete media (DMEM/F12 supplemented with 5% horse serum, 20 ng/mL EGF, 10 µg/ml insulin, 0.5 µg/ml hydrocortisone, 0.1 µg/ml cholera toxin, and 1X antibiotic/antimycotic). For experiments under growth factor-depleted conditions, MCF10A cells were grown in DMEM/F12 supplemented with 1% charcoal/dextran-stripped serum (CSS), 0.5 µg/ml hydrocortisone, 0.1 µg/ml cholera toxin, and 1X Antibiotic-Antimycotic. Cell lines were routinely evaluated for *Mycoplasma* contamination. All experiments were completed less than 2 months after establishing stable cell lines or thawing early-passage cells.

Mouse models

All animal experiments were approved by the UTSW Institutional Animal Care and Use Committee (IACUC protocol 2018-102535). SA493 breast cancer PDXs (*ER*⁺/*HER2*^{S310F}) were obtained from Samuel Aparicio (Eirew et al., 2015).

METHOD DETAILS

Database searches

The Foundation Medicine database was queried for breast cancers harboring co-occurring mutations in *ERBB2* and *ERBB3* in January 2019. Breast cancers from METABRIC (n=2509), Broad (n=103), Sanger (n=100), TCGA (n=1108), INSERM Metastatic Breast Cancer (n=216), and the Metastatic Breast Cancer Project (n=237) were queried in April 2019 using www.cBioPortal.org (Cerami et al., 2012). Breast cancers from Project GENIE from Centers reporting alterations in *ERBB2* and *ERBB3* (n=8545; Centers = COLU, CRUK, DFCI, DUKE, MSK, PHS, UCSF, VHIO, VICC, and YALE) were queried in June 2019 using www.cBioPortal.org/GENIE.

(Consortium, 2017). All breast cancers with co-occurring *ERBB2* and *ERBB3* mutations were cross-referenced using at least two additional mutations in other genes to ensure that individual patients were not counted more than once.

Computational modeling

Structural modeling of proteins was carried out using the Rosetta 3.12 macromolecular modeling software package (Bender et al., 2016; Leman et al., 2020). The RosettaLigand application was used for molecular docking (Combs et al., 2013; Meiler and Baker, 2005). Molecular dynamics simulations were carried out using AMBER 18 (Case et al., 2018). Protein-protein interaction energy was obtained using the InterfaceAnalyzer mover in Rosetta. Protein-ligand interaction energy was estimated using MMPBSA.py (Miller et al., 2012). RMSD, atom-atom distances, and dihedrals angles were obtained using various applications: AmberTools18, CPPTRAJ (Roe and Cheatham, 2013), and Rosetta. We used the following forcefields / score functions for molecular modeling and simulation: AMBER ff14SB for proteins (Maier et al., 2015), generalized AMBER force field 2 (GAFF2) for ligands (neratinib), REF2015 for Rosetta kinase domain modeling, and Franklin 2019 for Rosetta HER2/HER3 near-full-length heterodimer modeling. Neratinib geometry optimization was performed with Gaussian 09 at the B3LYP/6-31G* level of theory. The electrostatic surface potential (ESP) was estimated with HF/6-31G* calculation. Partial charges generated with Gaussian 09 were fit to neratinib for MD simulations with the RESP procedure in AmberTools18 (Cornell et al., 1993). All structures were rendered with PyMOL 2.2. Graphs were generated with Matplotlib.

Structural modeling of the HER2-HER3 heterodimer

Modeling of the HER2/HER3 heterodimer was carried out in the Rosetta package (Song et al., 2013) utilizing multi-template comparative modeling (RosettaCM) with PDB structures 4RIW and 3PP0 as templates (Aertgeerts et al., 2011; Littlefield et al., 2014). HER3 was retained from 4RIW. The HER2 sequence was threaded on the receiver kinase EGFR structure from 4RIW during templated modeling, or was templated on the HER2 structure from 3PP0 superimposed on EGFR from 4RIW. In both instances, fragments from either structure were incorporated during RosettaCM refinement. Following the comparative modeling step, each structure underwent a single repeat of constrained FastRelax in the REF2015 score function. A total of 5000 structures were generated, and the top 20 best scoring structures were subjected to FastRelax with five repeats and constraints on starting coordinates. Constraints were ramped down during FastRelax. The best scoring complex was taken for subsequent analysis.

The near-full-length HER2/HER3 heterodimer was constructed with RosettaCM multi-template modeling. The HER2/HER3 KD heterodimer generated in the previous step, which included the juxtamembrane B (JMB) region, was used for the most of the intracellular component. C-terminal tails were excluded from modeling because they are primarily disordered. The transmembrane domain (TMD) and juxtamembrane A (JMA) regions were modeled based on the EGFR homodimer NMR structural ensemble in PDB ID 2M20. The HER2 extracellular domain (ECD) domains I – III were modeled from the HER2 crystallographic structure PDB ID 1N8Z. The HER3 ECD domains I – II were modeled from the EGFR crystallographic structure PDB ID 3NJP with fragments from the HER3 tethered structure PDB ID 1M6B. The PDB ID 1HAE NMR ensemble of Neuregulin 1 (NRG1) was superimposed with EGF from 3NJP prior to incorporation into the model of HER3 ECD. The ECD domain IV was modeled from 3NJP for both HER2 and HER3. Initial threaded models of each of these structures were combined with the Rosetta Domain Assembly application (Koehler Leman and Bonneau, 2018). Subsequently, the assembled structure underwent iterative rounds of all-atom minimization in the Franklin2019 score function with POPC implicit membrane and ramped constraints to start coordinates (weights successively lowered: 1.0, 0.5, 0.1, 0.0). The minimized structure was relaxed with constraints to start coordinates. Each domain (KD, JM, TM, and ECD) were separately and successively relaxed to produce 100 structures in each round, after which the best scoring structure was moved to the next round. The final structure was relaxed with constraints ramped down before being used in subsequent Rosetta mutational studies.

The fully inactivated HER2^{WT} monomeric KD were generated with RosettaCM utilizing a structure of EGFR in the inactive state (PDB ID 3GT8) and refined with three independent 2.0 μ s MD simulations. Structure snapshots were nominally collected every 20 ns from each trajectory and relaxed without constraints. The best scoring relaxed structure was taken to be the inactive HER2 conformation for steered MD and umbrella sampling simulations.

Molecular docking of HER2 protein and ligand (neratinib)

The initial structure of the inhibitor neratinib was downloaded from the PubChem database. The structures were then optimized using Gaussian 09 D.01 version at b3lyp/6-31G(d)* level. Electrostatic potential charges were calculated using Gaussian 09 and assigned using AmberTools18. Small molecule conformers were generated with the BioChemical Library (BCL) conformer generator using default settings to create a maximum of 100 conformers (Mendenhall et al., 2020). Ligand (neratinib) docking was carried out using the RosettaLigand application in Rosetta 3.12 (Combs et al., 2013; DeLuca et al., 2015; Meiler and Baker, 2005; Smith and Meiler, 2020). The docking of ligands into proteins is divided into two phases: low resolution docking and high resolution docking. During the low-resolution docking phase, each ligand is allowed to explore the binding site in a 6.0 Å radius. Rigid body transformation is combined with ligand conformation swaps for 500 cycles of Monte Carlo Metropolis optimization. During the high-resolution docking phase, 6 cycles of side-chain rotamer and ligand conformer sampling were coupled with 0.2 Å in a Monte Carlo simulated annealing algorithm. 5000 docked protein-ligand complexes were generated. The interface score of the protein-ligand complex was calculated using the InterfaceAnalyzer mover in Rosetta 3.12 and the “ligand.wts” score weights. The root-mean-square deviation was computed using the lowest interface scored structure as the reference pose.

Classical MD simulations

Structures from the above modeling methods were used as an initial structure for further studies. The active and inactive reference frames of HER2 were set using previous studies and allowed to equilibrate based in our classical MD simulations. Each structure was solvated in a rectangular TIP3P box (12 Å buffer) neutralized with monovalent ions Cl^- and Na^+ ions (Vega and Abascal, 2011). Solvent molecules were minimized with 2,000 steps of steepest gradient descent followed by 5,000 steps of conjugate gradient descent, while the protein/protein-ligand complex was restrained. The protein/protein-ligand complex was minimized in 2,000 steps of steepest gradient descent followed by 5,000 steps of conjugate gradient descent. Restraints were subsequently removed and the whole system underwent 2,000 steps of steepest gradient descent followed by 5,000 steps of conjugate gradient descent minimization. The system was slowly heated in NVT ensemble to 100K over 100 ps. The system was then heated in NPT ensemble at 1 bar from 100K to physiologic temperature (310K) over 500 ps. Equilibration was performed in NPT ensemble at 310K for 100 ns with a Monte Carlo barostat. The temperature was controlled using Langevin dynamics and a unique random seed was used for each simulation. SHAKE was implemented to constrain bonds involving hydrogen atoms. Periodic boundary conditions were applied and the particle mesh Ewald (PME) algorithm was adopted for the calculation of long-range electrostatic interactions with a cutoff distance of 10 Å. Hydrogen mass repartitioning was employed to allow an integration time step of 4 fs.

Conformational free energy calculations

Potential of mean force (PMF) profiles for the active – inactive conformational transition in HER2 monomeric KD were obtained by performing constant velocity steered MD (SMD) and Umbrella sampling (US) simulations prior to free energy determination with the weighted histogram analysis method (WHAM) as implemented by Alan Grossfield (Grossfield,). SMD simulations were performed over 100 ns with a harmonic bias potential and spring constant of 500 kcal/mol/Å². SMD simulations were performed in both directions (from the active to the inactive state and vice versa) using the C α RMSD to the reference coordinates as the collective variable. A minimum of 250 windows were selected from each forward and backward simulation with which to seed US simulations, such that each US simulation contained at least 500 windows to ensure overlap. A 2D harmonic restraining potential was applied to two CVs for the US simulations. CV1 (y-axis) was defined as the difference in the distance between R868(NE, CZ, NH1, NH2) – E770(OE1, OE2) and K753(NZ) – E770(OE1, OE2). CV2 (x-axis) was defined as the dihedral angle formed by the C α atoms of the following residues: D863, F864, G865, and L866. A 2.0 kcal/mol/Å² spring constant was used for CV1, and a 10.0 kcal/mol/rad² spring constant was used for CV2. At each umbrella center a 5 ns simulation was performed. The first 1 ns was used for equilibration, and the following 4 ns were used for analysis in WHAM. Lowest free energy pathway (LFEP) analysis completed with the LFEP package freely available from the Moradi Laboratory at the University of Arkansas.

Protein-ligand free energy calculations

Protein-ligand binding free energy calculations were performed with MM/GBSA implemented in the AmberTools18 MMPBSA.py (Miller et al., 2012). Trajectories were stripped of water and ions. Energies were computed with a surface tension of 0.0072 kcal/mol/Å² and salt concentration of 0.15 M. The non-polar contribution to the solvation free energy was approximated using the LCPO method (Weiser et al., 1999). Default radii assigned with Leap were kept for GBSA calculations. The enthalpic and solvation free energy contributions were computed every 100 ps. All calculations were completed from three independent trajectories and averaged.

Protein-protein interface energy

The protein-protein interface energy, or $\Delta G_{\text{dimerization}}$, was determined using a modified version of the Cartesian $\Delta\Delta G$ protocol from Frenz et al. (Frenz et al., 2020). The best scoring HER2^{WT}/HER3^{WT} KD heterodimer comparative model was transferred to the REF2015_Cartesian score function to an additional 20 rounds of FastRelax. The best scoring model from this subset was passed to the Cartesian $\Delta\Delta G$ application in Rosetta with interface mode enabled in order to generate optimized models for HER2^{WT}/HER3^{WT}, HER2^{L755S}/HER3^{WT}, HER2^{V777L}/HER3^{WT}, HER2^{L869R}/HER3^{WT}, HER2^{WT}/HER3^{E928G}, HER2^{L755S}/HER3^{E928G}, HER2^{V777L}/HER3^{E928G}, and HER2^{L869R}/HER3^{E928G}. The backbone degrees of freedom were set to $i \pm 1$ from the mutation site and 5 iterations were performed for each mutation. The all-atom attractive energy and solvation implicit energy score terms were given cutoffs of 9.0 Å. Finally, an additional 100 structures were generated for each heterodimer KD complex by performing unrestrained Cartesian FastRelax beginning with the best scoring model by the “dG_separated” score term from the InterfaceAnalyzer mover (repacking both monomers after separation). Final binding affinity estimates for each complex are obtained by averaging the top 20 best structures by “dG_separated” from the final round of relax. Results are reported as mean \pm standard error over those 20 models.

Plasmids

The Gateway Cloning system (Thermo Fisher Scientific) was used to generate pLX302-HER2 and pLX304-HER3 plasmids. The pDONR-223 vector encoding either HER2^{WT} or HER3^{WT} was subjected to site-directed mutagenesis (Genewiz) to generate HER2 or HER3 mutants. HER2^{WT} and mutant plasmids were recombined into the lentiviral expression vector pLX-302 containing a C-terminal V5 epitope tag and puromycin resistance marker. HER3^{WT} and mutant plasmids were recombined into pLX-304, also containing a C-terminal V5 tag, and blasticidin resistance marker. pFlag-CMV5.1 HER2 WT and HER3 WT ICDs were described previously (Hanker et al., 2017) and were subjected to site-directed mutagenesis (Genewiz) to generate mutants.

Transient transfections

Transient transfections were performed using Lipofectamine 2000 (Thermo Fisher Scientific) according to the manufacturer's instructions. Co-transfection of pFlag-CMV5.1 *HER2* and *HER3* WT and mutant ICDs was performed as described (Red Brewer et al., 2013). siRNA transfections were performed using Lipofectamine RNAiMAX Transfection Reagent (Thermo Fisher Scientific) according to the manufacturer's instructions.

Lentiviral infections

Lentiviral supernatant was produced in early-passage 293FT cells by transfection with psPAX2 and pMD2.G packaging plasmids along with the appropriate pLX302-*HER2* or pLX304-*HER3* plasmid. Target cells or organoids were spin-infected the next day with viral supernatant in the presence of 8 $\mu\text{g}/\text{ml}$ polybrene. Two d later, target cells/organoids were selected with puromycin (MCF10A: 2 $\mu\text{g}/\text{ml}$; OVCAR8: 0.7 $\mu\text{g}/\text{ml}$; MCF7: 0.5 $\mu\text{g}/\text{ml}$; SA493 organoids: 1 $\mu\text{g}/\text{ml}$) and/or 10 $\mu\text{g}/\text{ml}$ blasticidin for at least 4 d. Stable cell lines were maintained in media containing puromycin and/or blasticidin.

Immunoprecipitation

If cells were pre-treated with antibodies (trastuzumab/pertuzumab), prior to lysis, cells were incubated with cold acid wash buffer (0.5 mol/L NaCl, 0.2 mol/L Na acetate, pH 3.0) for 6 min to remove bound antibodies. Monolayers were then washed 3 times with ice-cold PBS. Cell lysates were harvested using ice ND lysis buffer [1% Triton X100, 20 mM Tris HCl, 150 mM NaCl, supplemented with 1X protease inhibitor (Roche) and phosphatase inhibitor (Roche) cocktails] and rotated at 4°C for 1 h. Lysates were then clarified by spinning at 10,000 \times g at 4°C for 15 min. Protein concentrations were measured using BCA standard curves (Pierce). Four-eight μL of *HER2* Ab-17 antibody (Thermo Fisher Scientific) was added to 500–1000 μg protein lysate and rotated at 4°C overnight. IP was carried out using the Invitrogen Dynabeads Protein G Immunoprecipitation Kit (10007D) as directed. Lysates were next subjected to SDS-PAGE and immunoblot analysis. Each immunoprecipitation experiment was performed a minimum of two times.

Proximity ligation assay

MCF10A cells (5 \times 10⁴ cells/well) were seeded in 8-well chamber slides (Lab-Tek, 177445) in triplicate and incubated in EGF/insulin-free media + 1% CSS overnight. PLA was performed with Duolink In Situ Red Starter Kit Mouse/Rabbit (Sigma) using mouse anti-*HER2* (Thermo Fisher Scientific; Cat# MS-730-P1-A) and rabbit anti-*HER3* (Cell Signaling Technologies; Cat# 12708) antibodies according to the manufacturer's protocol and then imaged with a DMI8 inverted microscope (Leica). The number of PLA foci per cell was quantified using ImageJ as described (Prado Martins et al., 2018). A minimum of 7 images per sample were analyzed.

Western blot analysis

Prior to lysing, organoids were dissociated into single cell suspension by mechanical shearing and enzymatic digestion using TrypLE express (Gibco, #12604021). Adherent cells or organoid cell pellets were washed with ice-cold PBS and lysed with RIPA buffer (Sigma) supplemented with 1X protease inhibitor (Roche) and phosphatase inhibitor (Roche) cocktails. Lysates were centrifuged at 13,500 rpm for 15 min. Protein concentrations in supernatants were quantified using BCA protein assay kit (Pierce). 20–40 μg of total protein was fractionated on bis-tris 4–12% gradient gels (NuPAGE) and transferred to nitrocellulose membranes (BioRad). Membranes were blocked with 5% non-fat dry milk/TBST at room-temperature for 1 h, followed by overnight incubation with primary antibodies of interest at 4°C in 5% BSA/TBST. All antibodies were purchased from Cell Signaling – P-*HER2* Y1221/2 (#2243; 1:500), *HER2* (#2242; 1:1000), P-*HER3* Y1197 (#4561; 1:500), P-*HER3* Y1289 (#4791; 1:500), P-*HER3* Y1197, *HER3* (#12708; 1:1000), P-AKT S473 (#9271; 1:500), P-AKT T308 (#13038; 1:500), P-S6 S235/6 (#2211; 1:1000), PS6 S240/4 (#2215; 1:1000), P-ERK T202/Y204 (#9101; 1:1000), and β -actin (#4970; 1:1000). Membranes were cut horizontally to probe with multiple antibodies. In some cases, P-Akt S473, P-Erk, and P-S6 S240/244 antibodies were combined during primary incubation. Nitrocellulose membranes were washed and incubated with HRP-conjugated α -rabbit or α -mouse secondary antibodies for 1 h at room temperature. Protein bands were detected with an enhanced chemiluminescence substrate (Perkin Elmer) using the ChemiDoc Imaging System (Bio-Rad). Immunoblots were quantified using ImageJ.

Flow cytometry

HER-2 cell surface staining was performed with the trastuzumab antibody. MCF10A stable cells (8 \times 10⁵) were incubated with 0.2 $\mu\text{g}/\text{ml}$ trastuzumab for 30 min at 4°C. Cells were washed in FACS buffer (Thermo Scientific) then incubated with an Alexa Fluor 647-conjugated goat anti-human IgG secondary antibody (Thermo Scientific; 1 $\mu\text{g}/\text{ml}$) for 30 min at 4°C. After 2 additional washes, the cells were analyzed on an LSR Fortessa flow cytometer (BD Biosciences). Ten thousand cellular events were analyzed per sample. Data were analyzed using FlowJo software (BD Biosciences).

Organoid establishment and culture

Fresh/frozen tumor chunks from SA493 (*HER2*^{S310F}) PDXs were rinsed twice with 10 ml AdDF+++ media (advanced DMEM/F12 containing 1X Glutamax, 10 mM HEPES and antibiotics) and minced into 1–2 mm pieces. 10 ml dissociation media (1:1 vol/vol F12, DMEM supplemented with 2% w/v bovine serum albumin, 300 U/ml collagenase, 100 U/ml hyaluronidase, 10 ng/ml epidermal growth factor (EGF), 1 mg/ml insulin, and 0.5 mg/ml hydrocortisone) was added to tumor fragments and incubated for 2 hr at

37°C with constant shaking at 275 rpm. Dissociated tumor fragments were centrifuged at 1200 rpm for 5 min and subjected to RBC lysis as per manufacturer's protocol (BD Biosciences), if the cell pellet was visibly red. Tumor fragments were further dissociated by adding 3 ml pre-warmed trypsin and incubating in a 37°C bead bath for 5–7 min. 6 ml neutralization solution (2% FBS in PBS) was added and centrifuged at 1200 rpm for 5 min. Tumor pellets were then treated with the Dispase/DNAse cocktail for 5–7 min at 37°C, and neutralized and centrifuged as above. Tumor cell suspension was subjected to magnetic separation of CD298+ human cells (biotin-conjugated α -CD298 antibody, Miltenyi Biotec, #130-101-292) to eliminate potential mouse cell contamination, using EasySep human biotin positive selection kit II (STEMCELL technologies #17663). The cell pellet was resuspended in appropriate volume of cold BME and 40 ml of cell suspension was added to the center of each well of a 24-well plate and allowed to solidify by placing in a 37°C incubator for 20 min. 500 ml organoid medium (DMEM/F12 containing 250 ng/ml R-Spondin 3, 5 nM Neuregulin 1, 5 ng/ml FGF7, 20 ng/ml FGF10, 5 ng/ml EGF, 100 ng/ml Noggin, 500 nM A83-01, 5 μ M Y-27632, 500 nM SB202190, 1X B27 supplement, 1.25 mM N-Acetylcysteine, 5 mM Nicotinamide, 1X GlutaMax, 10 mM Hepes, 50 μ g/ml primocin, and 100 U/ml penicillin/100 μ g/ml streptomycin) was added to each well and the plate was returned to a 37°C incubator maintained at 2% O₂ level.

For viability assays, established organoids were dissociated into single cell suspension by mechanical shearing and enzymatic digestion using TrypLE express (Gibco, #12604021). Dissociated cells were resuspended in 100 ml of cold organoid media containing 5% BME and 1000 cells/well were seeded into BME-coated 96-well plate in organoid media lacking EGF and NRG1. The next day, organoid cultures were treated with drugs and the effect on viability was assessed 6 d later using CellTiter-Glo 3D viability assay kit (Promega # G9681). Organoids were photographed using a Leica DMI1 inverted microscope.

Sanger sequencing of *ERBB2* and *ERBB3*

RNA was isolated from CW2 cells using the Maxwell RSC simplyRNA Cells Kit (Promega) on the Maxwell RSC Instrument (Promega). RNA was isolated from SA493 organoids using the Qiagen RNeasy Micro Kit. Reverse transcription was performed using the iScript cDNA Synthesis Kit (Bio-Rad). The appropriate regions of *ERBB2* and *ERBB3* were PCR-amplified using the following primers: 5' GCCTGCCTCCACTTCAACCA (*ERBB2*_forward; S310F), 5' GTAAGTCCCTCACCTCTCG (*ERBB2*_reverse; S310F), 5' GTGAA GGTGCTTGATCTGG (*ERBB2*_forward; L755S), 5' ATCTGCATGGTACTCTGTCT (*ERBB2*_reverse; L755S), 5' TGAGGCCGATAT TGGAACGG (*ERBB3*_forward), and 5' AGGTTGGGCGAATGTTCTCA (*ERBB3* reverse). Sanger sequencing for *ERBB2*^{S310F}, *ERBB2*^{L755S}, and *ERBB3* was performed using the 5' CATCTGTGAGCTGCACTGCC, 5' GTTGGGACTCTTGACCAGCA, and 5' GTGCATAGAAACCTGGCTGC sequencing primers, respectively.

Quantitative RT-PCR

Total RNA was isolated using the Maxwell RSC simplyRNA Cells Kit (Promega) on the Maxwell RSC Instrument (Promega). cDNA was synthesized using the iScript cDNA synthesis Kit (Bio-Rad) and then subjected to qPCR using PowerUp SYBR Green Master Mix (Thermo Fisher Scientific) and Qiagen RT² qPCR primer assays for human *ERBB2*, *ERBB3*, and *YWHAZ* (housekeeping control). To specifically detect *ERBB2*^{2264T>C} (L755S), the following qPCR primers were used: 5'CAGTGGCCATCAACGTGTC (forward) and 5'TACACCAGTTCAGCAGGTCCT (reverse). qPCR was performed using the QuantStudio3 Real-Time PCR System (Thermo Fisher Scientific).

Cell viability assay and IC₅₀ estimation

Cell viability was determined using the Cell Titer Glo assay (Promega) according to the manufacturer's instructions. Briefly, single-cell suspensions were generated by straining trypsinized cells through a 40 μ m cell strainer (Fisher Scientific). 500–1000 cells per well were plated in 96-well white clear-bottom plates in quadruplicate. Cells were treated with 10 concentrations of inhibitor or vehicle alone at a final volume of 150 μ L per well. After 6 d of treatment, 25 μ L of Cell Titer Glo was added to each well. Plates were shaken for 15 min, and bioluminescence was determined using the GloMax Discover Microplate Reader (Promega). Blank-corrected bioluminescence values were normalized to DMSO-treated wells and normalized values were plotted in GraphPad Prism using non-linear regression fit to normalized data with a variable slope (four parameters). IC₅₀ values were calculated by GraphPad Prism at 50% inhibition.

Cell proliferation assay

CW2 cells were transfected with Control or HER3 siRNA in triplicate. Four d after transfection, cells were trypsinized and counted with a Z2 Coulter Counter Analyzer (Beckman coulter).

Three-dimensional morphogenesis assay

Cells were seeded on growth factor-reduced Matrigel (BD Biosciences) in 48-well plates following published protocols (Debnath et al., 2003). Inhibitors were added to the medium at the time of cell seeding. Fresh media and inhibitors were replenished every 3 d. Following 7–10 d, colonies were stained with 5 mg/ml MTT for 20 min. Plates were scanned and colonies measuring \geq 100 μ m were counted using GelCount software (Oxford Optronix). Colonies were photographed using a Leica DMI1 inverted microscope.

Cell invasion assay

Transwell invasion assays were performed using BioCoat Growth Factor Reduced Matrigel Invasion Chambers (Corning) according to the manufacturer's instructions. Briefly, MCF10A cells were seeded at 100,000 cells/well in serum-free DMEM/F12

media. DMEM/F12 media containing 5% FBS was added to the bottom chamber as a chemoattractant. The cells were incubated under the desired conditions and 22 h later, cells that invaded to the underside of the membrane were stained with 0.5% crystal violet. Transwells were photographed using a Leica DMI1 inverted microscope. Brightfield images were quantified using ImageJ software. Images were converted to RGB stack. The green channel was thresholded and filtered (3 pixels) to remove the pores. The total thresholded area was measured.

Xenograft Studies

CW2 cells were re-suspended in serum-free RPMI and Growth Factor-Reduced Matrigel (1:1 ratio) and injected subcutaneously into the right flank of 4–6 week old female athymic nu/nu mice (Envigo). When the average tumor volume reached $\sim 200 \text{ mm}^3$, mice received daily doses of vehicle (0.5% Methylcellulose + 0.4% Tween 80, orogastric gavage), neratinib (40 mg/kg; orogastric gavage), alpelisib (30 mg/kg; orogastric gavage), or neratinib + alpelisib. In our previous studies, we have found neratinib to cause anorexia and moderate body weight loss. To avoid these toxicities, all mice were prophylactically supplemented with DietGel 76A (Clear H₂O) in addition to regular chow. Tumor diameters were measured twice weekly using calipers and tumor volumes were calculated using the formula: $\text{volume} = \text{width}^2 \times \text{length} / 2$.

QUANTIFICATION AND STATISTICAL ANALYSIS

Statistical analysis was performed using GraphPad Prism 8.1.2. For analyses involving multiple comparisons, one-way or two-way (for grouped bar graphs) ANOVA with Bonferroni posthoc test was used. Otherwise student's t-test was used. Bar graphs show mean \pm S.E.M. The neratinib/alpelisib combination index was calculated using the Chou-Talalay test (Chou, 2010).